A high-order robust subcell monolithic DG/FV formulation for nonlinear shallow-water equations on unstructured grids

Sacha Cardonna, Fabien Marche & François Vilar

May 22, 2026

Abstract. In this work, we propose a new high-order numerical method for the two-dimensional nonlinear shallow-water (NSW) equations on unstructured meshes. The approach is based on the subcell monolithic DG/FV method, recently introduced in [75], in which higher-order Discontinuous Galerkin (DG) schemes are blended, at the subcell scale, with lowest-order robust Finite Volume (FV) methods. This is made possible through the reformulation of high-order DG schemes as a FV-like schemes defined on a subgrid, through the introduction of some particular fluxes referred to as *reconstructed fluxes*. The strategy then relies on the introduction of blended numerical fluxes, defined as convex combinations of reconstructed high-order DG fluxes and robust first-order FV ones. The blending coefficients are locally computed at each subcell interface in order to enforce unavoidable nonlinear stability properties. This allows the scheme to remain stable in the presence of strong gradients, shocks, and wet-dry fronts, while still keeping high-order accuracy in smooth regions. A particular attention is paid to the discrete formulation associated with the bathymetry source term. The scheme is designed to be well-balanced for motionless steady-states, thanks to some fine tuning of local hydrostatic-like reconstructions, respectively applied at two different scales and on two different kinds of approximations: i) at the level of DG fluxes between elements, focusing on suitable reconstructions of high-order polynomial traces, ii) at the level of FV fluxes between subcells, focusing on the reconstruction of subcell piecewise-constant values. This innovative two-levels reconstruction ensures that motionless steady states are not only exactly preserved on fully unstructured meshes, but also down to the subcell scale. This new numerical method relies on a fully *a priori* treatment, and does not require any *a posteriori* re-computing and adapting steps, while remaining conservative by construction. Several numerical experiments illustrate its ability to accurately capture multidimensional wet-dry interfaces, to control spurious oscillations near classical discontinuities, and accurately resolve localized flow-features inside relatively large mesh elements.

Contents

Introduction

The nonlinear shallow-water (NSW) equations remain one of the most prominent mathematical models for describing flows in hydraulic, geophysical or coastal engineering. Compared to more complex weakly dispersive models such as Boussinesq-type equations, the hyperbolic nature of the NSW system allows accurate descriptions of several important features like trans-critical evolution or steep-fronted flows, includinf, for instance, dam-breaks, flood waves, and bore propagation in nearshore zones. Consequently, this model is largely used in numerical models to predict coastal inundations and investigate complex wave run-up and run-down dynamics over coastal structures, see for instance [28, 36, 47].

To approximate the weak solutions of the NSW equations, a wide variety of numerical methods have been developed since the 1960s. These range from Finite-Volume (FV) [2, 3, 7, 27, 29, 77] and Finite-Element (FE) methods [6, 59, 63, 72], to spectral or pseudo-spectral methods [40, 53, 61]. Among them, Godunov-type FV schemes are particularly well-regarded, as their robust shock-capturing capabilities and minimal computational cost are essential for maintaining the physical integrity of sharp gradients [4, 8, 11, 15, 31, 41, 51, 55, 60, 67, 71]. However, standard FV methods are fundamentally limited by low-order accuracy, unless they rely on heavily extended, and therefore computationally expensive, reconstruction stencils.

Discontinuous Galerkin (DG) methods have therefore gained significant attraction for approximating hyperbolic Partial Differential Equations (PDEs). They successfully bridge the geometric flexibility of FE methods with the local conservation properties of FV schemes [19, 48, 66]. DG methods allow for arbitrary spatial order of accuracy on compact stencils, easily support highly unstructured geometries, and are naturally suited for h/p adaptation and concurrent programming. Yet, higher-order DG methods for nonlinear hyperbolic problems are notoriously prone to Runge phenomenon and nonlinear stability issues, generally producing spurious oscillations in the presence of discontinuities, steep gradients or local physical constraints. In the context of the NSW equations, it may obviously compromise the computation of positive water-height near wet-dry fronts.

To address these stability issues without loosing the benefits of high-order accuracy, numerous limiting or corrections strategies have been explored. These generally fall into *a priori* and *a posteriori* paradigms. *A priori* approaches preemptively apply corrections based on troubled-cell indicators [64] using artificial viscosity [34, 42, 62, 73], moment limiters [10, 17, 22, 43, 50], (H)WENO reconstructions [5, 65, 81, 82], or subcell FV shock-capturing techniques [14, 18, 70]. Alternatively, *a posteriori* methods compute a candidate solution first and locally recompute it with a robust low-order scheme if admissibility criteria (e.g., positivity) are violated [16, 20, 21, 23, 30, 39, 54]. Unfortunately, both correction strategies typically modify the polynomial globally within the troubled cells, which inevitably degrades the scheme's resolution on coarse multidimensional meshes.

Recently, local subcell conservative methods have emerged, focusing on the accuracy preservation at smaller scales [74, 76], that is to say within the resolution of suitable subgrids. Applied to the NSW equations [37, 38], such approaches may locally modify the numerical solution, at the subcell level, through specific flux corrections. Expanding on this idea to avoid *a posteriori* computations, a novel class of *a priori* local subcell monolithic DG/FV schemes is recently introduced in [75] for homogeneous hyperbolic systems. In parallel, other monolithic strategies have been developed to blend high-order schemes with low-order convex methods. This includes continuous Galerkin discretizations [46, 58] and DG spectral-element methods (DGSEM) [52, 68, 69, 78]. However, recent approaches relying on Summation-By-Parts (SBP) and flux collocation are, at least for the time-being, restricted to 1D or extended cartesian tensor-product grids, even though some extensions to unstructured triangular meshes have recently been proposed [78].

In this paper, in the continuity of [12] which focused on the 1D NSW model, we introduce here a two-dimensional monolithic DG/FV subcell convex property-preserving scheme for the 2D NSW equations on unstructured grids. The idea is to reinterpret higher-order DG formulations as FV-like schemes defined on a sub-partition of each element, through the introduction of particular fluxes referred to as reconstructed fluxes, while the proposed global approximation framework naturally allows for very general subcell shapes. From this, the core of our strategy relies on the construction and fine tuning of blended numerical fluxes, as convex combinations of reconstructed high-order DG interface fluxes and robust first-order FV fluxes. The corresponding blending coefficients are space and time adaptively computed, both at the sub-grid scale and sub-time stages, in order to enforce key admissibility constraints such as strict water-height positivity while expecting to maintain the highest possible level of space and time accuracy.

Another key feature of the proposed method is the treatment of source terms in hyperbolic systems of conservation laws, which must be fully compatible with the new subcell monolithic *a priori* discretization of numerical fluxes. For the NSW equations, the spatially varying bathymetry source term requires exactly balancing flux gradients and topography variations at the discrete level. While numerous low- and high-order methods have been developed to address this challenge within FV, FE, or DG frameworks (see, e.g., [24,56,80]), we propose a novel 2D two-level hydrostatic reconstruction strategy. Inspired by the well-balanced well-known formulations of [51] and extending the 1D ideas from [12], our approach applies flow-state reconstructions to both local sub-mean values at the sub-partition level and local high-order polynomial traces at the global mesh level, combined with a dedicated subcell source term discretization. This new 2D two-scale strategy consistently preserves the required balance within the monolithic blending procedure, exactly maintaining motionless steady states down to the subcell level.

Extensive numerical evaluations confirm that our discrete framework reliably replicates expected flow features, including wet-dry fronts. Notably, the model captures fine-scale local behaviors even within coarse mesh elements, without compromising high-order accuracy in smooth zones.

1. Continuous and discrete settings

1.1. The 2D nonlinear shallow-water equations

Given a smooth parameterization b of the bathymetry variation, denoting the free-surface elevation by η, the water discharge by $\mathbf{q} = (q_x, q_y)^\top$ and $\mathbf{u} = (u_x, u_y)^\top$ as the depth-averaged water velocity, the 2D pre-balanced NSW are commonly written as follows

$$\begin{cases} \partial_t \eta + \nabla_{\boldsymbol{x}} \cdot \mathbf{q} = 0, \\ \partial_t \mathbf{q} + \nabla_{\boldsymbol{x}} \cdot \big(\mathbf{u} \otimes \mathbf{q} + \frac{g\eta}{2}(\eta - 2b)\mathbb{I}_2\big) = \mathbf{S}^{\mathbf{q}}[\tau](\mathbf{v}), \end{cases}$$

or in a compact form

$$\partial_t \mathbf{v} + \nabla_{\boldsymbol{x}} \cdot \mathbb{F}(\mathbf{v}, b) = \mathbf{S}[\tau](\mathbf{v}), \tag{1}$$

supplemented with some initial-data $\mathbf{v}(\cdot, 0) := \mathbf{v}^0$ and where:

- $\mathbb{R}^2 \times \mathbb{R}_+ \ni (\boldsymbol{x}, t) \mapsto \mathbf{v}(\boldsymbol{x}, t) := (\eta, q_x, q_y)(\boldsymbol{x}, t) \in \mathscr{H}_b^+$ gathers the chosen flow description variables, with
$$\mathscr{H}_b^+ = \{(\eta, q_x, q_y) \in \mathbb{R}^3 \mid H := \eta - b \geq 0\},$$
- $\mathscr{H}_b^+ \times \mathbb{R} \ni (\mathbf{v}, b) \mapsto \mathbb{F}(\mathbf{v}, b) := \big(\mathbf{q},\, \mathbf{u} \otimes \mathbf{q} + \frac{g\eta}{2}(\eta - 2b)\mathbb{I}_2\big)^\top \in \mathscr{M}_{3\times 2}(\mathbb{R})$ is the (nonlinear) flux function, given in the pre-balanced form [51]
- $\mathscr{H}_b^+ \ni \mathbf{v} \mapsto \mathbf{S}[\tau](\mathbf{v}) := (0, S^{\mathbf{q}}[\tau](\mathbf{v}))^\top \in \mathbb{R}^3$ denotes a generic algebraic source term depending on external data τ. Relevant choices include:
  - $\mathscr{H}_b^+ \ni \mathbf{v} \mapsto \mathbf{B}[b](\mathbf{v}) := (0, -g\eta\, \nabla_{\boldsymbol{x}} b)^\top$ describes the effect of bathymetric variations,
  - $\mathscr{H}_b^+ \ni \mathbf{v} \mapsto \mathbf{R}[\mathrm{n_f}](\mathbf{v}) := \Big(0,\, -\mathrm{n_f^2} \frac{\mathbf{q}\|\mathbf{q}\|}{(\eta - b)^\gamma}\Big)^\top$ denotes a nonlinear (quadratic) friction source term, with $\gamma \geq 0$ a user-defined exponent (e.g. $\gamma = 7/3$ for Manning's formulation),
  - $\mathscr{H}_b^+ \ni \mathbf{v} \mapsto \mathbf{R}^{\mathrm{lin}}[\mathrm{n_f}](\mathbf{v}) := (0, -\mathrm{n_f}\mathbf{q})^\top$ is a linear (laminar) friction source term.

  These source terms may be considered independently or combined.

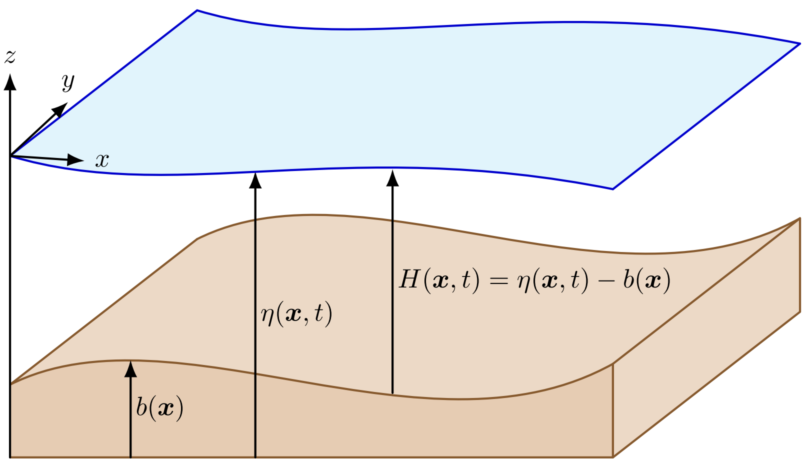

Figure 1: Schematic representation of the 2D shallow-water flow configuration, illustrating the free surface elevation $\eta(\boldsymbol{x},t)$, the bathymetry $b(\boldsymbol{x})$, and the water height $H(\boldsymbol{x},t)$.

1.2. Discrete framework

Domain partitioning and related polynomial approximation

We denote by $\Omega \subset \mathbb{R}^2$ the computational domain, which is assumed to be a bounded open set with Lipschitz boundary $\partial\Omega$. We denote by $\mathcal{T}_h$ a triangulation of Ω into $n_{\rm el}$ open cells ω_c, $c \in \llbracket 1, n_{\rm el} \rrbracket$, such that

$$\overline{\Omega} = \bigcup_{\omega_c \in \mathcal{T}_h} \overline{\omega_c}, \quad \text{and} \quad \mathring{\omega}_c \cap \mathring{\omega}_v = \emptyset, \ \text{ for all } c \neq v.$$

Given $\omega_c \in \mathcal{T}_h$, we denote by h_c a measure of its diameter, and define $h := \max_{c \in \llbracket 1, n_{\rm el} \rrbracket} h_c$ as the diameter of the largest cell in the mesh. Similarly, $\boldsymbol{x}^c_{\rm b} := (x^c_{\rm b}, y^c_{\rm b})$ denotes the barycenter of ω_c, and h^c_x (resp. h^c_y) stands for measures of ω_c x- (resp. y-) lengths in both cartesian directions.

The set of all mesh faces is denoted by $\mathcal{F}_h := \mathcal{F}^0_h \cup \mathcal{F}^\partial_h$, where $\mathcal{F}^0_h$ collects the internal faces and $\mathcal{F}^\partial_h$ the boundary faces. For each cell $\omega_c \in \mathcal{T}_h$, we denote by $\mathcal{F}_c := \{\Gamma \in \mathcal{F}_h \mid \Gamma \subset \partial\omega_c\}$ the set of local faces. During our numerical investigations, we consider simplicial meshes, i.e. $\#\mathcal{F}_c = 3$ for all $\omega_c \in \mathcal{T}_h$, but the method can of course be extended to more general elements. If $\Gamma \in \mathcal{F}_c$, we define $\mathbf{n}_{c\Gamma}$ as the unit normal to Γ pointing outward from ω_c. For internal faces $\Gamma \in \mathcal{F}^0_h$, we fix an arbitrary but consistent orientation and denotes the associated unit normal vector by $\mathbf{n}_\Gamma$. For boundary faces $\Gamma \in \mathcal{F}^\partial_h$, we set $\mathbf{n}_\Gamma := \mathbf{n}_{c\Gamma}$. If there is no ambiguity, we will often denote $\mathbf{n}_{cv}$ as the normal vector associated to the face Γ_{cv} of the element ω_c shared with its neighbor ω_v.

For any integer $k \geq 0$, let us define the space of piecewise-polynomials on the mesh elements, called broken-polynomials space for short:

$$\mathbb{P}^k(\mathcal{T}_h) := \{v \in L^2(\Omega) \mid \forall \omega_c \in \mathcal{T}_h, \ v_{|\omega_c} \in \mathbb{P}^k(\omega_c)\},$$

where $\mathbb{P}^k(\omega_c)$ denotes the space of polynomials in ω_c of total degree at most k, with $N_k := \dim \mathbb{P}^k(\omega_c) = (k+1)(k+2)/2$. Piecewise polynomial functions belonging to some broken-polynomial space $\mathbb{P}^k(\mathcal{T}_h)$ are denoted with a subscript h in the following, and for any $v_h \in \mathbb{P}^k(\mathcal{T}_h)$, and for all $\omega_c \in \mathcal{T}_h$, we use the shortcut $v^c_h := v_{h_{|\omega_c}}$. We set $\mathbf{P}^k(U) := (\mathbb{P}^k(U))^3$ for any relevant domain U (e.g., $U = \mathcal{T}_h$, $\mathcal{F}_h$, ω_c etc.). A basis for $\mathbb{P}^k(\omega_c)$ is denoted by

$$\boldsymbol{\Psi}_c := \{\psi^c_j\}_{j \in \llbracket 1, N_k \rrbracket}, \tag{2}$$

and for $v^c_h \in \mathbb{P}^k(\omega_c)$, $\underline{v}^c := \{\underline{v}^c_j \mid j \in \llbracket 1, N_k \rrbracket\}$ stand for the *local* degrees of freedom associated with ω_c. We also denote by $\underline{v} := \{\underline{v}^c \mid c \in \llbracket 1, n_{\rm el} \rrbracket\}$ the *global* degrees of freedom of v_h. For $\omega_i \in \mathcal{T}_h$, we denote by p^k_c the L^2-orthogonal projector onto $\mathbb{P}^k(\omega_c)$ and p^k_h the global L^2-orthogonal projector onto $\mathbb{P}^k(\mathcal{T}_h)$, gathering all the local L^2 projectors p^k_c. We also define a gradient operator $\nabla^k_h \colon \mathbb{P}^k(\mathcal{T}_h) \to \mathbb{P}^{k-1}(\mathcal{T}_h)$ such that, for all $v_h \in \mathbb{P}^k(\mathcal{T}_h)$:

$$(\nabla^k_h v_h)_{|\omega_c} := \nabla_{\boldsymbol{x}}(v^c_h), \qquad \forall \omega_c \in \mathcal{T}_h.$$

Seeking for approximate solutions of (1), the next sections are devoted to the computation of $\mathbf{v}_h := (\eta_h, \mathbf{q}_h)$, such that for any time value, $\mathbf{v}_h(\cdot, t) \in \mathbf{P}^k(\mathcal{T}_h)$, with the corresponding approximate local solution $\mathbf{v}_h^c$

$$\mathbf{v}_h^c(\boldsymbol{x}, t) = \sum_{m=1}^{N_k} \underline{\mathbf{v}}_m^c(t)\psi_m^c(\boldsymbol{x}). \tag{3}$$

Similarly, we set $b_h^c(\boldsymbol{x}) := \sum_{m=1}^{N_k} \underline{b}_m^c \phi_m^c(\boldsymbol{x})$. Lastly, for $\mathbf{v}_h \in \mathbf{P}^k(\mathcal{T}_h)$ and any related interface $\Gamma_{cv(k)}$, and when no confusion is possible, let us simply denote by $\mathbf{v}_k^-$ and $\mathbf{v}_k^+$, respectively, the interior and exterior traces with respect to ω_c of $\mathbf{v}_h^c$ and $\mathbf{v}_h^v$ to Γ_{cv}.

Sub-mesh and related discrete operators

Let us divide the initial mesh into subcells: for any given mesh element $\omega_c \in \mathcal{T}_h$, we introduce a sub-partition $\mathcal{T}_c^{\text{sub}}$ into N_s open disjoint subcells:

$$\overline{\omega}_c = \bigcup_{m \in [\![1, N_s]\!]} \overline{S}_m^c,$$

where the subcell S_m^c has the area $|S_m^c|$, gathered in the diagonal area matrix $\mathbb{D}_c \in \mathcal{M}_{N_s}(\mathbb{R})$ s.t. $\mathbb{D}^c := \text{diag}_{m \in [\![1, N_s]\!]}(|S_m^c|)$.

Remark 1.1. *For the numerical applications considered in this work, only two particular subdivision families are considered: a hybrid quadrilateral/triangle configuration and a fully triangular one. However, any subdivision that satisfies the required properties described later can be used, allowing for very general subcell shapes, see [75, 76] for more details.*

In what follows, Γ_{mp}^c refers to the face between subcell S_m^c and its neighbor S_p, and its length is denoted by ℓ_{mp}. For a given cell ω_c and a subcell S_m^c, we denote by $\mathcal{F}_m^c$ the set of faces of S_m^c and we set $n_f^m := \#\mathcal{F}_m^c$, while n_f^c refers to the number of subcell's faces which lies in the interior of ω_c (and therefore not belonging to $\partial\omega_c$). The set $\mathcal{V}_m^c$ contains the face-neighboring subcells of S_m^c (s.t. $\#\mathcal{V}_m^c = n_f^m$), while $\breve{\mathcal{V}}_m^c$ is the set of face-neighboring subcells of S_m^c belonging to ω_c (we recall that a sub-neighbor S_p can be either inside cell ω_c i.e. $S_p \in \mathcal{T}_c^{\text{sub}}$ (then $S_p = S_p^c$), or in one of its neighboring cells ω_v i.e. $S_p \in \mathcal{T}_v^{\text{sub}}$ (then $S_p = S_p^v$), see Fig. 2).

We denote by $\mathbf{n}_{mp}$ the unit normal vector to the face Γ_{mp}^c of S_m^c shared with $S_p^v \in \mathcal{V}_m^c$, oriented with the following sign function ε_{mp}^c:

$$\varepsilon_{mp}^c := \begin{cases} 1 & \text{if } S_p \in \breve{\mathcal{V}}_m^c \text{ are neighbors and } m < p, \\ -1 & \text{if } S_p \in \breve{\mathcal{V}}_m^c \text{ are neighbors and } m > p, \\ 0 & \text{if } S_p \notin \mathcal{V}_m^c. \end{cases}$$

The set of vertices $\boldsymbol{x}_p$ of subcell S_m^c is denoted by $\mathcal{P}_m^c$, $\mathcal{V}_p$ is the set of subcells that share $\boldsymbol{x}_p$ as a vertex and the set

$$\mathcal{N}(S_m^c) := \bigcup_{\boldsymbol{x}_p \in \mathcal{P}_m^c} \mathcal{V}_p,$$

gathers the S_m^c and its node-neighboring subcells S_p^v (without discriminating the owning global elements). Finally, the set $\mathcal{V}_{mp}$ contains all the subcells that shares at least one vertex with the face Γ_{mp}.
For any given $\omega_c \in \mathcal{T}_h$, the set of piecewise-constant functions on the sub-mesh is:

$$\mathbb{P}^0(\mathcal{T}_c^{\text{sub}}) := \{v \in L^\infty(\omega_c) \mid \forall S_m^c \in \mathcal{T}_c^{\text{sub}},\ v_{|S_m^c} \in \mathbb{P}^0(S_m^c)\},$$

and we introduce the family of subcell-indicator functions

$$\{\mathbb{1}_m^c \mid m \in [\![1, N_s]\!]\},$$

such that $\mathbb{1}_m^c(\boldsymbol{x}) := 1$ if $\boldsymbol{x} \in S_m^c$, and 0 otherwise, allowing to define the (mean-value) projector $\overline{\pi}_c^k$ onto $\mathbb{P}^0(\mathcal{T}_c^{\text{sub}})$ such that

$$\mathbb{P}^k(\omega_c) \ni v_h^c \mapsto \overline{\pi}_c^k \circ v_h^c := \sum_{m=1}^{N_s} \overline{v}_m^c \mathbb{1}_m^c =: \overline{v}_h^c \in \mathbb{P}^0(\mathcal{T}_c^{\text{sub}}),$$

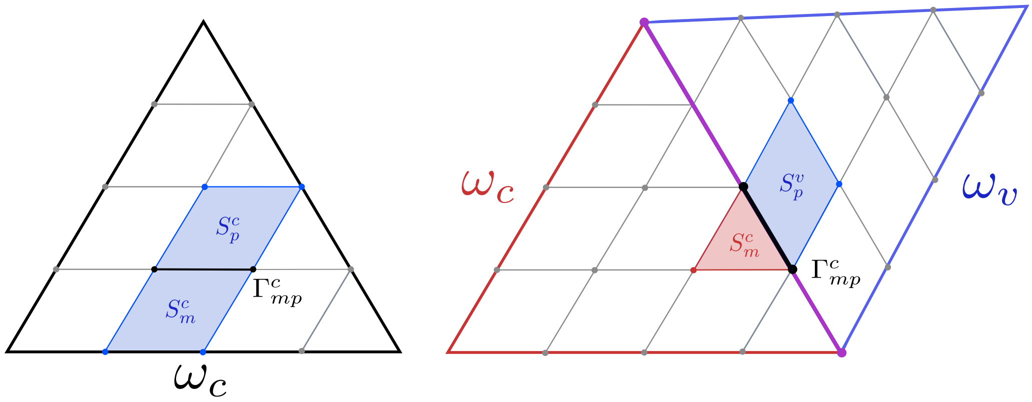

Figure 2: Two cases: subneighbor S_p inside cell ω_c (left), and subneighbor S_p inside neighbor cell ω_v (right).

where

$$\{\overline{v}_m^c \mid m \in [\![1, N_s]\!]\} =: \overline{v}^c$$

is the collection of piecewise-constant components defined as the mean-values of v_h^c on the subcells belonging to $\mathcal{T}_c^{\text{sub}}$, and called *sub-mean values*. Note that, in what follows and when no confusion is possible, $\overline{v}^c$ may be seen as a vector of $\mathbb{R}^{N_s}$, a set of N_s mean-values or identified with the associated piecewise-constant function $\overline{v}_h^c \in \mathbb{P}^0(\mathcal{T}_c^{\text{sub}})$. In order to reach a global description of subcells and related operators, we gather the local subcells partitions and define the associated global approximation space as follows:

$$\widetilde{\mathcal{T}_h} := \bigcup_{\omega_c \in \mathcal{T}_h} \mathcal{T}_c^{\text{sub}}, \qquad \mathbb{P}^0(\widetilde{\mathcal{T}_h}) := \bigtimes_{\omega_c \in \mathcal{T}_h} \mathbb{P}^0(\mathcal{T}_c^{\text{sub}}).$$

The global projector onto $\mathbb{P}^0(\widetilde{\mathcal{T}_h})$, obtained by gathering the local ones $\overline{\pi}_c^k$, is denoted by $\overline{\pi}_h^k$. In what follows, piecewise-constant functions belonging to $\mathbb{P}^0(\widetilde{\mathcal{T}_h})$ are denoted with an overline and a subscript h, and for any $\overline{v}_h \in \mathbb{P}^0(\widetilde{\mathcal{T}_h})$, and for all $S_m^c \in \widetilde{\mathcal{T}_h}$, we obviously have the identity $\overline{v}_m^c = \overline{v}_{h|S_m^c}$.

Remark 1.2. *For the coupling between the classical DG schemes and the subcell FV-like method, the projection operator* $\overline{\pi}_c^k : \mathbb{P}^k(\omega_c) \to \mathbb{P}^0(\mathcal{T}_c^{\text{sub}})$ *must be injective. This naturally requires the number of polynomial degrees of freedom* N_k *to be less than or equal to the number of subcells per cell* N_s *(*$N_k \leq N_s$*). This injectivity ensures that the polynomial moments can be uniquely recovered from the subcell mean values. The associated local transformation matrix* $\mathbb{P}_c = \left(\pi_{mp}^c\right)_{(m,p)} \in \mathscr{M}_{N_s \times N_k}(\mathbb{R})$ *is defined as*

$$\pi_{mp}^c = \frac{1}{|S_m^c|} \int_{S_m^c} \varphi_p^c(\boldsymbol{x}) \,\mathrm{d}\boldsymbol{x}, \qquad \forall (m,p) \in [\![1, N_s]\!] \times [\![1, N_k]\!].$$

For our subdivision to be admissible, $\mathbb{P}_c$ *must have full column rank. This guarantees the existence of a reconstruction operator* $\mathbb{R}_c$ *acting as a left inverse, such that* $\mathbb{R}_c\mathbb{P}_c = \mathbb{I}_{N_k}$*. These operators are then used to switch between the polynomial representation of the solution and its subcell mean values:*

$$\overline{v}^c = \mathbb{P}_c\, \underline{v}^c \quad \textit{and} \quad \underline{v}^c = \mathbb{R}_c\, \overline{v}^c.$$

When $N_s > N_k$*, the reconstruction problem is overdetermined. To properly recover the polynomial moments* $\underline{v}^c$ *from the subcell averages* $\overline{v}^c$*, we rely on a least-squares procedure, defining the reconstruction operator as the pseudo-inverse:*

$$\mathbb{R}_c := \left(\mathbb{P}_c^\top \mathbb{P}_c\right)^{-1} \mathbb{P}_c^\top.$$

In the light of [1, 76], a subdivision is then admissible if and only if $\mathbb{P}_c^\top \mathbb{P}_c$ *is indeed invertible. Of course the reconstruction operator* $\mathbb{R}_c$ *simply reduces to* $\mathbb{P}_c^{-1}$ *when* $N_s = N_k$*. Note that these local problems can be easily vectorized on modern computational ressources.*

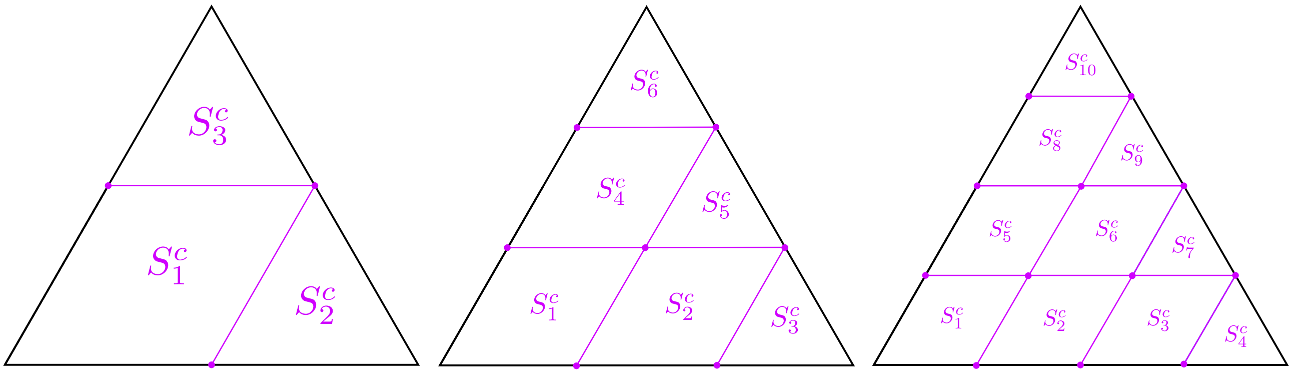

Figure 3: Partition of a mesh element ω_c into $N_s = N_k$ subcells for $\mathbb{P}^1$ (left), $\mathbb{P}^2$ (center) and $\mathbb{P}^3$ (right) cases.

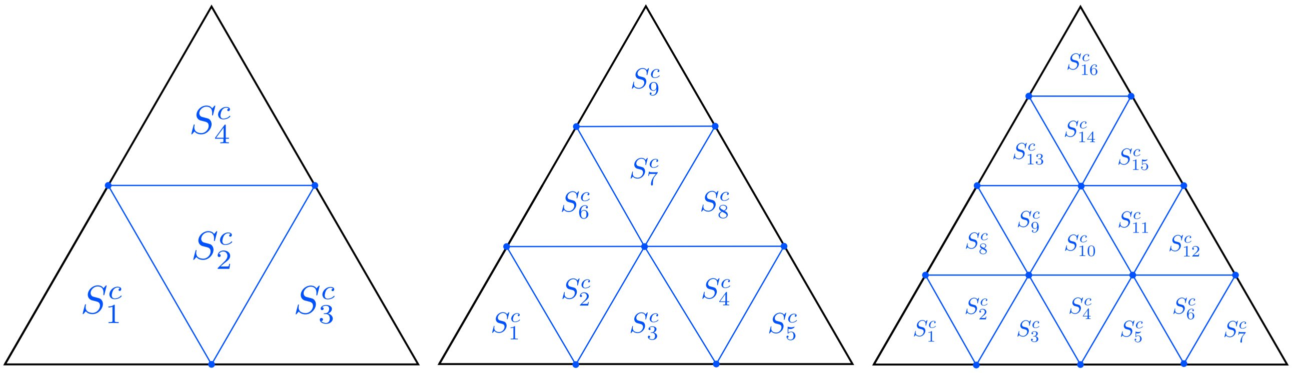

Figure 4: Partition of a mesh element ω_c into $N_s > N_k$ subcells for $\mathbb{P}^1$ (left), $\mathbb{P}^2$ (center) and $\mathbb{P}^3$ (right) cases.

Time discretization and time-marching algorithm.

Given a final time $T > 0$, we consider a general partition of the time interval $[0, T]$ defined by $0 =: t^0 < t^1 < \cdots < t^n < \cdots < t^N := T$. The time step is denoted by $\Delta t^n \in \mathbb{R}_+^*$ and may vary with time, such that for any $n \geq 0$, we have $t^{n+1} = t^n + \Delta t^n$. Time integration is performed using explicit *Strong Stability Preserving Runge-Kutta* (SSP-RK) schemes [32].

Introducing the time-stepping procedure naturally leads to a few additional time-related notations. We define $\mathbf{v}_h^n := \mathbf{v}_h(\cdot, t^n)$, and let $\overline{\mathbf{v}}_h^n := \overline{\pi}_h^k \circ \mathbf{v}_h^n =: (\overline{\eta}_h^n, \overline{\mathbf{q}}_h^n)$ denote the associated piecewise-constant function over the sub-mesh. For each cell ω_c, we denote

$$\overline{\mathbf{v}}^{c,n} := \{\overline{\mathbf{v}}_m^{c,n} \mid m \in [\![1, N_s]\!]\},$$

as the set of sub-mean values at time t^n, where each $\overline{\mathbf{v}}_m^{c,n}$ corresponds to the value of $\overline{\mathbf{v}}_h^n$ restricted to S_m^c. When the context is clear, we may omit the superscripts c and n to simplify notation.

Considering the semi-discrete formulation written in operator form,

$$\partial_t \mathbf{v}_h + \mathscr{A}_h(\mathbf{v}_h) = 0,$$

where $\mathscr{A}_h$ is a nonlinear operator, the third-order SSP-RK method advances the solution from time level n to $n + 1$ through the following stages:

$$\begin{aligned}
\mathbf{v}_h^{n,1} &= \mathbf{v}_h^n - \Delta t^n \mathscr{A}_h(\mathbf{v}_h^n), \\
\mathbf{v}_h^{n,2} &= \frac{1}{4}(3\mathbf{v}_h^n + \mathbf{v}_h^{n,1}) - \frac{\Delta t^n}{4}\mathscr{A}_h(\mathbf{v}_h^{n,1}), \\
\mathbf{v}_h^{n+1} &= \frac{1}{3}(\mathbf{v}_h^n + 2\mathbf{v}_h^{n,2}) - \frac{\Delta t^n}{3}\mathscr{A}_h(\mathbf{v}_h^{n,2}),
\end{aligned}$$

where $\mathbf{v}_h^{n,1}$ and $\mathbf{v}_h^{n,2}$ are intermediate stage values. The precise definition of the initial-data $\mathbf{v}_h^0$ is temporarily postponed, as one has to account for consistency and balancing with the bathymetric source term discretization.

The time step Δt^n is adaptively computed according to the following CFL condition, relying on the subcells geometry and the maximum wave speed computed from the sub-mean values of the solution:

$$\Delta t^n = \frac{\displaystyle\min_{\omega_c \in \mathcal{T}_h,\, S_m^c \in \mathcal{T}_c^{\mathrm{sub}}} |S_m^c|}{\displaystyle\sigma \max_{\omega_c \in \mathcal{T}_h} \left(\sum_{k=1}^{\#\mathcal{F}_c} \ell_{cv(k)} \right)}, \qquad \sigma = \max_{\omega_c \in \mathcal{T}_h} \left[\max_{S_m^c \in \mathcal{T}_c^{\mathrm{sub}},\, S_p^v \in \mathcal{V}_m^c} \left(|\overline{\mathbf{u}}_m^c \cdot \mathbf{n}_{mp}| + \sqrt{\mathrm{g}\overline{H}_m^c} \right) \right], \tag{4}$$

2. Discrete formulations and flux reconstruction

In this section, we focus on the discrete formulations associated with (1). In the following, and when no confusion is possible, ω_v refers to a generic face-neighbor of ω_c and we introduce the following shortcut for the normal component of the physical flux across the (oriented) face Γ_{cv}:

$$\mathbb{F}_{cv}^* := \mathbb{F}(\mathbf{v}_h, b_h)_{|\Gamma_{cv}} \cdot \mathbf{n}_{cv}.$$

To approximate $\mathbb{F}_{cv}^*$, we may use any consistent and positive numerical flux $\mathbb{F}_{cv}^{*,\mathrm{DG}}$, like the global Lax-Friedrichs (LF) numerical flux for instance.

2.1. Discontinuous Galerkin (DG) formulation

A semi-discrete global DG formulation of the NSW equations with topography source term may reads as: find $\mathbf{v}_h := (\eta_h, \mathbf{q}_h) \in \mathbf{P}^k(\mathcal{T}_h)$ such that, for all $\varphi_h \in \mathbb{P}^k(\mathcal{T}_h)$,

$$\sum_{\omega_c \in \mathcal{T}_h} \int_{\omega_c} \partial_t \mathbf{v}_h \varphi_h \, \mathrm{d}\boldsymbol{x} - \sum_{\omega_c \in \mathcal{T}_h} \int_{\omega_c} \mathbb{F}(\mathbf{v}_h, b_h) \cdot \nabla_{\boldsymbol{x}} \varphi_h \, \mathrm{d}\boldsymbol{x} + \sum_{\omega_c \in \mathcal{T}_h} \sum_{\Gamma \in \mathcal{F}_c} \int_\Gamma \mathbb{F}_\Gamma^{*,\mathrm{DG}} \varphi_h \, \mathrm{d}s = \sum_{\omega_c \in \mathcal{T}_h} \int_{\omega_c} \mathbf{B}[b_h](\mathbf{v}_h) \varphi_h \, \mathrm{d}\boldsymbol{x}. \tag{5}$$

At the element level, testing against basis functions (2) and replacing $\mathbf{v}_h^c$ by its polynomial expansion, we obtain the following semi-discrete formulation for the polynomial moments $\underline{\mathbf{v}}^c = \{\underline{\mathbf{v}}_m^c \mid m \in [\![1, N_k]\!]\}$:

$$\sum_{m=1}^{N_k} \frac{\mathrm{d}\underline{\mathbf{v}}_m^c}{\mathrm{d}t} \int_{\omega_c} \psi_m^c \psi_p^c \, \mathrm{d}\boldsymbol{x} - \int_{\omega_c} \mathbb{F}(\mathbf{v}_h^c, b_h^c) \cdot \nabla_{\boldsymbol{x}} \psi_p^c \, \mathrm{d}\boldsymbol{x} + \sum_{\Gamma \in \mathcal{F}_c} \int_\Gamma \mathbb{F}_\Gamma^{*,\mathrm{DG}} \psi_p^c \, \mathrm{d}s = \int_{\omega_c} \mathbf{B}[b_h^c](\mathbf{v}_h^c) \psi_p^c \, \mathrm{d}\boldsymbol{x}. \tag{6}$$

This formulation may also be written in a compact matrix-vector form as follows

$$\mathbb{M}_c \frac{\mathrm{d}\underline{\mathbf{v}}^c}{\mathrm{d}t} = \Phi_c + \mathbf{S}_c, \tag{7}$$

where:

- $\mathbb{R}^{N_k} \ni \Phi_c$ is the DG residual defined as follows:

$$(\Phi_p^c)_{p \in [\![1, N_k]\!]} := - \sum_{\Gamma \in \mathcal{F}_c} \int_\Gamma \mathbb{F}_\Gamma^{*,\mathrm{DG}} \psi_p^c \, \mathrm{d}s + \int_{\omega_c} \mathbb{F}(\mathbf{v}_h^c, b_h^c) \cdot \nabla_{\boldsymbol{x}} \psi_p^c \, \mathrm{d}\boldsymbol{x},$$

- $\mathcal{M}_{N_k}(\mathbb{R}) \ni \mathbb{M}_c$ is the mass matrix, with $(\mathbb{M}_{mp}^c)_{(m,p) \in [\![1, N_k]\!]^2} := \int_{\omega_c} \psi_m^c \psi_p^c \, \mathrm{d}\boldsymbol{x}$,
- $\mathbb{R}^{N_k} \ni \mathbf{S}_c$ is the bathymetry source term, with $(\mathbf{S}_p^c)_{p \in [\![1, N_k]\!]} := \int_{\omega_c} \mathbf{B}[b_h^c](\mathbf{v}_h^c) \psi_p^c \, \mathrm{d}\boldsymbol{x}$.

2.2. Equivalency between DG and a subcell FV-like scheme

In this section, we reformulate the previous local DG scheme into a new formulation relying on submean values, and relying solely on the interior flux $\mathbb{F}(\mathbf{v}_h^c, b_h^c)$, along with a correction term that accounts for the jumps of the normal component approximations on cells interfaces.

Lemma 2.1. *The global semi-discrete DG formulation* (5) *is locally equivalent to the following formulation relying on submean values:*

$$\frac{\mathrm{d}\overline{\mathbf{v}}_m^c}{\mathrm{d}t} = -\frac{1}{|S_m^c|} \left(\sum_{S_p^v \in \mathcal{V}_m^c} \int_{\Gamma_{mp}^c} \mathbb{F}_h^c \cdot \mathbf{n}_{mp} \, \mathrm{d}s - \sum_{k=1}^{\#\mathcal{F}_c} \int_{\Gamma_{ij(k)}^c} \left(\mathbb{F}_h^c \cdot \mathbf{n}_{cv(k)} - \mathbb{F}_{cv(k)}^{*,\mathrm{DG}} \right) \widetilde{\psi}_m^c \, \mathrm{d}s \right) + \int_{S_m^c} \mathbf{B}_h^c \, \mathrm{d}\boldsymbol{x}$$

for all $m \in [\![1, N_s]\!]$*, with the sub-resolution spanning set of functions* $\widetilde{\boldsymbol{\Psi}}_{\omega_c} := \{\widetilde{\psi}^c_m\}_{m\in[\![1,N_s]\!]}$ *with* $\widetilde{\psi}^c_m(\boldsymbol{x}) = p^k_c \circ \mathbb{1}^c_m(\boldsymbol{x})$*, and where*

$$\mathbb{F}_h := p^k_h \circ \mathbb{F}(\mathbf{v}_h, b_h) \quad \textit{and} \quad \mathbf{B}_h := p^k_h \circ \mathbf{B}[b^c_h](\mathbf{v}^c_h),$$

the L^2*-projections of the flux function and source term onto* $\mathbb{P}^k(\mathscr{T}_h)$

Proof. Replacing the flux and source terms by their L^2-projections into (5), we get:

$$\int_{\omega_c} \partial_t \mathbf{v}^c_h \varphi^c_h \,\mathrm{d}\boldsymbol{x} - \int_{\omega_c} \mathbb{F}^c_h \cdot \nabla_{\boldsymbol{x}} \varphi^c_h \,\mathrm{d}\boldsymbol{x} + \sum_{k=1}^{\#\mathscr{F}_c} \int_{\Gamma_{cv(k)}} \mathbb{F}^{*,\mathrm{DG}}_{cv(k)} \varphi^c_h \,\mathrm{d}s = \int_{\omega_c} \mathbf{B}^c_h \varphi^c_h \,\mathrm{d}\boldsymbol{x}, \quad \forall \varphi^c_h \in \mathbb{P}^k(\omega_c).$$

Integrating by parts gives:

$$\int_{\omega_c} \partial_t \mathbf{v}^c_h \varphi^c_h \,\mathrm{d}\boldsymbol{x} - \sum_{k=1}^{\#\mathscr{F}_c} \int_{\Gamma_{cv(k)}} \left(\mathbb{F}^c_h \cdot \mathbf{n}_{cv(k)} - \mathbb{F}^{*,\mathrm{DG}}_{cv(k)} \right) \varphi^c_h \,\mathrm{d}s + \int_{\omega_c} \varphi^c_h \nabla_{\boldsymbol{x}} \cdot \mathbb{F}^c_h \,\mathrm{d}\boldsymbol{x} = \int_{\omega_c} \mathbf{B}^c_h \varphi^c_h \,\mathrm{d}\boldsymbol{x}, \qquad \forall \psi \in \mathbb{P}^k(\omega_c), \tag{8}$$

which is generally called the *strong DG form*. Since $\partial_t \mathbf{v}^c_h$, $(\nabla_{\boldsymbol{x}} \cdot \mathbb{F}^c_h)$, $\mathbf{B}^c_h \in \mathbf{P}^k(\omega_c)$, substituting $\widetilde{\psi}^c_m$ into (8) gives, for all $m \in [\![1, N_s]\!]$:

$$\int_{S^c_m} \partial_t \mathbf{v}^c_h \,\mathrm{d}\boldsymbol{x} = \sum_{k=1}^{\#\mathscr{F}_c} \int_{\Gamma_{cv(k)}} \left(\mathbb{F}^c_h \cdot \mathbf{n}_{cv(k)} - \mathbb{F}^{*,\mathrm{DG}}_{cv(k)} \right) \widetilde{\psi}^c_m \,\mathrm{d}s - \int_{S^c_m} \nabla_{\boldsymbol{x}} \cdot \mathbb{F}^c_h \,\mathrm{d}\boldsymbol{x} + \int_{S^c_m} \mathbf{B}^c_h \,\mathrm{d}\boldsymbol{x}.$$

We can then rewrite this with submean values, to get

$$\frac{\mathrm{d}\overline{\mathbf{v}}^c_m}{\mathrm{d}t} = -\frac{1}{|S^c_m|} \left(\sum_{S^v_p \in \mathscr{V}^c_m} \int_{\Gamma^c_{mp}} \mathbb{F}^c_h \cdot \mathbf{n}_{mp} \,\mathrm{d}s - \sum_{k=1}^{\#\mathscr{F}_c} \int_{\Gamma_{cv(k)}} \left(\mathbb{F}^c_h \cdot \mathbf{n}_{cv(k)} - \mathbb{F}^{*,\mathrm{DG}}_{cv(k)} \right) \widetilde{\psi}^c_m \,\mathrm{d}s \right) + \overline{\mathbf{B}}^c_m,$$

for all $m \in [\![1, N_s]\!]$, where $\overline{\mathbf{B}}^c_m$ and $\overline{\mathbf{v}}^c_m$ are respectively the submean values of $\mathbf{B}_h$ and $\mathbf{v}_h$ on subcell S^c_m. ☐

Lemma 2.2. *The reconstructed flux* $\widehat{\mathbb{F}}_c \in \mathbb{R}^{n^c_f}$ *such that*

$$\frac{\mathrm{d}\overline{\mathbf{v}}^c_m}{\mathrm{d}t} = -\frac{1}{|S^c_m|} \left(\sum_{S^v_p \in \mathscr{V}^c_m} \int_{\Gamma^c_{mp}} \widehat{\mathbb{F}}_n \,\mathrm{d}s \right) + \overline{\mathbf{B}}^c_m, \qquad \forall m \in [\![1, N_s]\!],$$

with

$$\sum_{S^v_p \in \mathscr{V}^c_m} \int_{\Gamma^c_{mp}} \widehat{\mathbb{F}}_n \,\mathrm{d}s = \sum_{S^v_p \in \mathscr{V}^c_m} \int_{\Gamma^c_{mp}} \mathbb{F}^c_h \cdot \mathbf{n} \,\mathrm{d}s - \sum_{k=1}^{\#\mathscr{F}_c} \int_{\Gamma_{cv(k)}} \left(\mathbb{F}^c_h \cdot \mathbf{n}_{cv(k)} - \mathbb{F}^{*,\mathrm{DG}}_{cv(k)} \right) \widetilde{\psi}^c_m \,\mathrm{d}s, \tag{9}$$

is equal to the DG numerical flux $\mathbb{F}^{*,\mathrm{DG}}_n$ *on the boundary* $\partial\omega_c$*, i.e.* $\widehat{\mathbb{F}}_{n|\partial\omega} = \mathbb{F}^{*,\mathrm{DG}}_n$*, and may be computed from the physical flux* $\mathbb{F}_c$ *through the following relation:*

$$\widehat{\mathbb{F}}_c = \mathbb{F}_c - \mathbb{A}^\top_c \mathscr{L}^{-1}_c \partial \mathbb{F}_c, \tag{10}$$

where:

- $\mathbb{R}^{n^c_f} \ni \mathbb{F}_c$ *collects the traces of the normal component of the interior flux on the sub-interfaces s.t. for all* $S^c_m \in \mathscr{T}^{\mathrm{sub}}_c$*,*

$$(\mathbb{F}^c_{mp})_{p\in[\![1,n^c_f]\!]} := \int_{\Gamma^c_{mp}} \mathbb{F}^c_h \cdot \mathbf{n}_{mp} \,\mathrm{d}s.$$

- $\mathscr{M}_{N_k \times n^c_f}(\mathbb{R}) \ni \mathbb{A}_c$ *stands for the adjacency matrix of cell* ω_c*, where*

$$\left(\mathbb{A}^c_{mp}\right)_{(m,p)\in[\![1,N_k]\!]\times[\![1,n^c_f]\!]} = \varepsilon^c_{mp},$$

- $\mathbb{R}^{N_s} \ni \partial \mathbb{F}_c$ *contains boundary contributions:*

$$(\partial \mathbb{F}^c_m)_{m \in [\![1, N_s]\!]} = \int_{\partial \omega_c} \left(\mathbb{F}^c_h \cdot \mathbf{n}_{\partial \omega_c} - \mathbb{F}^{*,\mathrm{DG}}_{\partial \omega_c} \right) \widehat{\psi}^c_m(s) \, \mathrm{d}s,$$

  where $\widehat{\psi}^c_m$ *is defined as follows:*

$$\widehat{\psi}^c_m(s) := \begin{cases} \widetilde{\psi}^c_m(s) & \text{if } s \in \partial \omega_c \setminus \partial S^c_m, \\ \widetilde{\psi}^c_m(s) - 1 & \text{if } s \in \partial \omega_c \cap \partial S^c_m. \end{cases}$$

- $\mathscr{M}_{n^c_f \times N_s}(\mathbb{R}) \ni \mathscr{L}_c^{-1}$ *is the inverse of the Laplacian matrix of the interior subgrid graph* $\mathbb{L}_c := \mathbb{A}_c^\top \mathbb{A}_c$ *on the orthogonal of its kernel. For any* $\lambda \neq 0$*, this generalized inverse writes:*

$$\mathscr{L}_c^{-1} = \left(\mathbb{L}_c + \lambda \Pi \right)^{-1} - \frac{1}{\lambda} \Pi \tag{11}$$

  with $\Pi = \frac{1}{N_s}(\mathbf{1} \otimes \mathbf{1}) \in \mathscr{M}_{N_k}(\mathbb{R})$*. In the numerical implementation, we typically choose* λ *to be equals to 1.*

Proof. See Appendix. ☐

We are then able to recast the semi-discrete DG formulation (5) into local subcell FV-like schemes, as follows:

Theorem 2.3. *For the NSW equations (1), considering any* $\varphi \in \mathbb{P}^k(\omega_c)$*, the classical DG formulation in cell* ω_c

$$\int_{\omega_c} \partial_t \mathbf{v}^c_h \varphi \, \mathrm{d}\boldsymbol{x} - \int_{\omega_c} \mathbb{F}(\mathbf{v}^c_h, b^c_h) \cdot \nabla_{\boldsymbol{x}} \varphi \, \mathrm{d}\boldsymbol{x} + \sum_{k=1}^{\#\mathscr{F}_c} \int_{\Gamma_{cv(k)}} \mathbb{F}^{*,\mathrm{DG}}_{cv(k)} \varphi \, \mathrm{d}s = \int_{\omega_c} \mathbf{B}[b^c_h](\mathbf{v}^c_h) \varphi \, \mathrm{d}\boldsymbol{x}, \tag{12}$$

can be recast into N_s *FV-like subcell schemes written as follows:*

$$\partial_t \overline{\mathbf{v}}^c_m = -\frac{1}{|S^c_m|} \sum_{S^v_p \in \mathscr{V}^c_m} \ell_{mp} \widehat{\mathbb{F}}_{mp} + \overline{\mathbf{B}}^c_m, \qquad \forall m \in [\![1, N_s]\!], \tag{13}$$

where the reconstructed flux is defined in (10).

Proof. The result is immediate from Lemmas 2.1 and 2.2. ☐

Remark 2.4. *Concerning the computation of velocity* $\mathbf{u} := \frac{\mathbf{q}}{H}$ *(whenever for polynomial values or piecewise constant subcell values), we use the following velocity regularization from [44] (omitting the indices for the sake of clarity):*

$$\mathbf{u} = \frac{\sqrt{2} H \mathbf{q}}{\sqrt{H^4 + \max(H^4, \varepsilon)}}, \qquad \mathbf{u}^{\mathrm{reg}} = \frac{\mathbf{q}}{H} \cdot \frac{\sqrt{2}}{\sqrt{1 + \frac{\varepsilon}{H^4}}}, \tag{14}$$

where ε *is a small, positive constant chosen a priori according to mesh scale and quality.*

3. Local subcell monolithic DG/FV scheme

3.1. High and low-order topography-dependent numerical fluxes

In the following, we rely on several numerical fluxes defined at both mesh and submesh interfaces. Due to the presence of non-flat bathymetry, in contrast with [75], the design of these fluxes must be carefully modified to ensure consistency, stability, preserve the expected high-order accuracy and, in particular, maintain the *well-balancing* property.

Inspired by the *hydrostatic reconstruction* for FV methods [4], extended to pre-balanced and DG formulations in [24, 51], a key feature of our approach is to finely tune this reconstruction to be strategically applied both on high-order polynomial traces or low-order approximations *both at cells and subcells levels*, using properly defined intermediate reconstructed states, in the same fashion as [12] for the 1D case. This involves non-conservative corrections to the numerical fluxes, which are designed to vanish at motionless steady states. As shown in previous works, these corrections do not affect the accuracy nor the consistency of the solution, and the conservation error is of the order of the scheme. Gathered with the previously introduced *reconstructed* fluxes used to relate high-order DG scheme to local lowest-order FV scheme, the construction of the local subcell monolithic DG/FV method is achieved through a combination of various numerical approximate interface fluxes. For clarity and ease of reference, the definitions of these numerical fluxes are gathered and summarized below:

- ♯ *global LF numerical flux with bathymetry variations.* The chosen interface flux has to account for the bathymetry variations from cell to cell or subcell to subcell, and is defined as follows:

$$(\mathscr{H}_b^+)^2 \times \mathbb{R}^4 \ni (\mathbf{v}^-, \mathbf{v}^+, b^-, b^+, \mathbf{n}) \mapsto \mathbb{F}^*(\mathbf{v}^-, \mathbf{v}^+, b^-, b^+, \mathbf{n}) := \frac{\mathbb{F}(\mathbf{v}^-, b^-) + \mathbb{F}(\mathbf{v}^+, b^+)}{2} \cdot \mathbf{n} - \frac{\sigma}{2}(\mathbf{v}^+ - \mathbf{v}^-), \tag{15}$$

- ♯ *high-order DG fluxes $\mathbb{F}^{*,\mathrm{DG}}_{cv(k)}$, $k \in [\![1, \#\mathcal{F}_c]\!]$ and cell-scale hydrostatic reconstruction.* Some local reconstructed interface values for the interface topography are considered, relying on the left and right traces of high-order approximations:

$$\widetilde{b}_k = \max\left(b_k^-, b_k^+\right), \qquad \check{b}_k = \widetilde{b}_k - \max\left(0, \widetilde{b}_k - \eta_k^-\right),$$

together with reconstructed interface values for the water-height and total elevation as follows:

$$\check{H}_k^\pm = \max\left(0, \eta_k^\pm - \widetilde{b}_k\right) \quad \text{and} \quad \check{\eta}_k^\pm = \check{H}_k^\pm + \widetilde{b}_k,$$

and interior/exterior solution values:

$$\mathbf{v}_k^\pm = \left(\check{\eta}_k^\pm, \frac{\check{H}_k^\pm}{H_k^\pm}\mathbf{q}_k^\pm\right)^\top.$$

Using these reconstructed values, we define the following (non-conservative) high-order interface flux through the interface between ω_c and $\omega_{v(k)}$ as follows:

$$\mathbb{F}^{*,\mathrm{DG}}_{cv(k)} = \mathbb{F}^*\left(\check{\mathbf{v}}_k^-, \check{\mathbf{v}}_k^+, \check{b}_k, \check{b}_k, \mathbf{n}_{cv(k)}\right) + \check{\mathbb{F}}^{\mathrm{DG}}_{cv(k)}, \tag{16}$$

where $\check{\mathbb{F}}^{\mathrm{DG}}_{cv(k)}$ is a correction term needed to ensure flux balancing at motionless steady states, defined as follows, inspired from [79]:

$$\check{\mathbb{F}}^{\mathrm{DG}}_{cv(k)} = \begin{pmatrix} 0 & 0 \\ \mathrm{g}\check{\eta}_k^-(\check{b}_k - b_k^-) & 0 \\ 0 & \mathrm{g}\check{\eta}_k^-(\check{b}_k - b_k^-) \end{pmatrix} \cdot \mathbf{n}_{cv(k)}.$$

- ♯ *first-order FV fluxes through subcells $\mathbb{F}^{*,\mathrm{FV}}_{mp}$, and subcell-scale hydrostatic reconstruction.* For a neighbor subcell S_p^v sharing a subface Γ_{mp}^c with S_m^c, we will denote by $\overline{\mathbf{v}}_m^c$ and $\overline{\mathbf{v}}_p^v$ respectively the interior and exterior mean-values with respect to Γ_{mp}^c. We then now proceed the same way as usual by new defining state reconstructions as follows:

$$\widetilde{\overline{b}}_{mp} = \max\left(\overline{b}_m^c, \overline{b}_p^v\right), \qquad \check{\overline{b}}_{mp} = \widetilde{\overline{b}}_{mp} - \max\left(0, \widetilde{\overline{b}}_{mp} - \overline{\eta}_m^c\right),$$
$$\check{\overline{H}}_m^c = \max\left(0, \overline{\eta}_m^c - \widetilde{\overline{b}}_{mp}\right), \qquad \check{\overline{H}}_p^v = \max\left(0, \overline{\eta}_p^v - \widetilde{\overline{b}}_{mp}\right),$$

and the reconstructed states for total elevation are then defined as

$$\check{\overline{\eta}}_m^c = \check{\overline{H}}_m^c + \check{\overline{b}}_{mp}, \qquad \check{\overline{\eta}}_p^v = \check{\overline{H}}_p^v + \check{\overline{b}}_{mp},$$

leading to new exterior and interior values:

$$\check{\overline{\mathbf{v}}}_m^c = \left(\check{\overline{\eta}}_m^c, \frac{\check{\overline{H}}_m^c}{\overline{H}_m^c}\overline{\mathbf{q}}_m^c\right)^\top, \qquad \check{\overline{\mathbf{v}}}_p^v = \left(\check{\overline{\eta}}_p^v, \frac{\check{\overline{H}}_p^v}{\overline{H}_p^v}\overline{\mathbf{q}}_p^v\right)^\top.$$

The corrected FV numerical flux writes then as

$$\mathbb{F}^{*,\mathrm{FV}}_{mp} = \mathbb{F}^*\left(\check{\overline{\mathbf{v}}}_m^c, \check{\overline{\mathbf{v}}}_p^v, \check{\overline{b}}_{mp}, \check{\overline{b}}_{mp}, \mathbf{n}_{mp}\right) + \check{\mathbb{F}}^{\mathrm{FV}}_{mp}, \tag{17}$$

where $\check{\mathbb{F}}^{\mathrm{FV}}_{mp}$ is the correction term assuring flux balancing at motionless steady states

$$\check{\mathbb{F}}^{\mathrm{FV}}_{mp} = \begin{pmatrix} 0 & 0 \\ g\check{\overline{\eta}}^{c}_{m}\left(\check{\overline{b}}_{mp} - b_{mp}\right) & 0 \\ 0 & g\check{\overline{\eta}}^{c}_{m}\left(\check{\overline{b}}_{mp} - b_{mp}\right), \end{pmatrix}$$

with b_{mp} denoting the mean-value of the bathymetry on cell ω_c at the face Γ^c_{mp}, i.e.

$$b_{mp} := \frac{1}{|S^c_m|} \int_{\Gamma^c_{mp}} b^c_h(s)\,\mathrm{d}s.$$

♯ *high-order DG reconstructed fluxes.* These fluxes are obtained in the previous section (10), within the formulation (9) and aim at locally mimicking the behavior of an "in-cell" FV scheme, while preserving the global high-order accuracy of the DG scheme in the encompassing mesh element:

$$\widehat{\mathbb{F}}_c = \mathbb{F}_c - \mathbb{A}_c^{\top} \mathscr{L}_c^{-1} \partial \mathbb{F}_c,$$

all the quantities in the above equation being defined in the previous section.

3.2. Blending high and low-order fluxes

The reformulations of the DG scheme into a subcell FV-like approach, achieved through the introduction of reconstructed fluxes and the first-order FV well-balanced corrected flux, now provide the foundation for constructing our monolithic FV subcell scheme, adapting the ideas of [75]. These schemes are convex combinations of high-order fluxes with robust low-order fluxes. Indeed, for every face Γ^c_{mp} of each subcell S^c_m, we compute the high-order DG reconstructed flux $\widehat{\mathbb{F}}_{mp}$ and the first-order robust FV numerical flux $\mathbb{F}^{*,\mathrm{FV}}_{mp}$. Then, those two quantities are gathered as follows:

$$\widetilde{\mathbb{F}}_{mp} = \mathbb{F}^{*,\mathrm{FV}}_{mp} + \Theta_{mp} \Delta \mathbb{F}_{mp}, \tag{18}$$

where $\Theta_{mp} \in [0, 1]$ and $\Delta \mathbb{F}_{mp} := \widehat{\mathbb{F}}_{mp} - \mathbb{F}^{*,\mathrm{FV}}_{mp}$. In the following, we refer to Θ_{mp} as *blending coefficients* and to $\widetilde{\mathbb{F}}_{mp}$ as *blended fluxes.*

Obviously, setting the blending coefficient to zero leads to a first-order FV numerical flux, while the value 1 gives the high-order DG reconstructed flux, leading to a local approximation equivalent to the usual DG formulation. For consistency reason, we define a unique blending coefficient for every subedge, meaning for every $S^v_p \in \mathscr{V}^c_m$, $\Theta_{mp} = \Theta_{pm}$. The local subcell monolithic DG/FV convex property preserving scheme for NSW then writes as

$$\frac{\mathrm{d}\overline{\mathbf{v}}^c_m}{\mathrm{d}t} = -\frac{1}{|S^c_m|} \sum_{S^v_p \in \mathscr{V}^c_m} \ell_{mp} \widetilde{\mathbb{F}}_{mp} + \overline{\mathbf{B}}^c_m. \tag{19}$$

Using a forward Euler time integration, we get the following:

Definition 3.1. *The subcell monolithic DG/FV convex property preserving scheme supplemented with a first-order time integration is*

$$\overline{\mathbf{v}}^{c,n+1}_m = \overline{\mathbf{v}}^{c,n}_m - \frac{\Delta t^n}{|S^c_m|} \sum_{S^v_p \in \mathscr{V}^c_m} \ell_{mp} \widetilde{\mathbb{F}}_{mp} + \Delta t^n \overline{\mathbf{B}}^{c,n}_m, \tag{20}$$

where $\widetilde{\mathbb{F}}_{mp} = \mathbb{F}^{*,\mathrm{FV}}_{mp} + \Theta_{mp}\left(\widehat{\mathbb{F}}_{mp} - \mathbb{F}^{*,\mathrm{FV}}_{mp}\right)$*, with the reconstructed high-order flux defined in* (10) *and the FV flux treated in* (17)*. In practice, higher-order strong stability preserving Runge-Kutta methods (SSP-RK) [33] are employed for time integration, as they can be seen as convex combination of Forward-Euler schemes.*

3.3. Source term discretization

As far as the source term discretization is concerned, we emphasize the issue of juggling between modal apprximations and piecewise-constant subcell values, in order to achieve a welcome well-balancing property for steady-states. Considering the topography source term $\mathbf{B}[b](\mathbf{v}) = (0, -\mathrm{g}\eta\nabla_{\boldsymbol{x}} b)^{\top}$, the proposed discretization should follow the following flowchart to ensure the consistency and balancing property with the discretization of the fluxes:

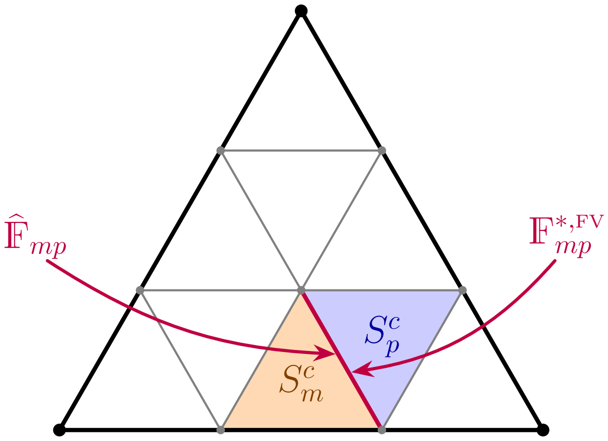

Figure 5: Representation of the two fluxes computed on each subinterface between two neighboring subcells S^c_m and S^v_p. The blending coefficient Θ_{mp} then allows to combine those two fluxes in a convex way to get the final flux $\widetilde{\mathbb{F}}_{mp}$ used in the monolithic scheme.

1. on each cell, subcell averages of b and η are computed. Using the projection matrix $\mathbb{P}_c$, b_h and η_h are reconstructed,
2. the source term is then projected onto $\mathbb{P}^k$ to obtain $\mathbf{B}_h := p^k_h \circ \mathbf{B}[b^c_h](\mathbf{v}^c_h)$,
3. the mean integral is computed and we get $\overline{\mathbf{B}}^c_m := \frac{1}{|S^c_m|}\int_{S^c_m} \mathbf{B}_h \,\mathrm{d}\boldsymbol{x}$.

From a practical viewpoint, and conveniently starting from a "classical" DG local approximation of the source term $\int_{\omega_c} \mathbf{B}_h\varphi_h \,\mathrm{d}x$, this may be formulated in a compact way using previously defined operators-matrix products:

$$\overline{\mathbf{B}}^c_m = \mathbb{P}_c\mathbb{M}_c^{-1}\left(\int_{\omega_c} \mathbf{B}_h\varphi_h \,\mathrm{d}x\right).$$

The reader may also find additional informations on this source term discretization process within subcell monolithic schemes in [12].

Remark 3.2. *Other discretizations are of course possible for the topography source term, like for example using the blending coefficients Θ in a mimetic way with the monolithic blended fluxes, representing the source term $\overline{\mathbf{B}}^c_m$ as a convex combination:*

$$\overline{\mathbf{B}}^c_m = \overline{\mathbf{B}}^{c,\mathrm{FV}}_m + \Theta^c_m\left(\overline{\mathbf{B}}^{c,\mathrm{DG}}_m - \overline{\mathbf{B}}^{c,\mathrm{FV}}_m\right),$$

with $\Theta^c_m := \frac{1}{\#\mathcal{V}^c_m}\sum_{S^v_p\in\mathcal{V}^c_m}\Theta_{mp}$, *and* $\overline{\mathbf{B}}^{c,\mathrm{DG}}_m = \frac{1}{|S^c_m|}\int_{S^c_m}\mathbf{B}_h\,\mathrm{d}\boldsymbol{x}$, *with for the FV source term :*

$$\overline{\mathbf{B}}^{c,\mathrm{FV}}_m = \frac{1}{|S^c_m|}\int_{S^c_m}\mathbf{B}[b^c_h](\overline{\mathbf{v}}^c_m)\,\mathrm{d}\boldsymbol{x} = -\frac{\mathrm{g}\overline{\eta}^c_m}{|S^c_m|}\int_{S^c_m}\begin{pmatrix}0\\ \nabla_{\boldsymbol{x}} b^c_h\end{pmatrix}\mathrm{d}\boldsymbol{x} = -\frac{\mathrm{g}\overline{\eta}^c_m}{|S^c_m|}\int_{\partial S^c_m}\begin{pmatrix}0\\ b^c_h\cdot\mathbf{n}\end{pmatrix}\mathrm{d}s,$$

or as in [26], i.e.

$$\overline{\mathbf{B}}^{c,\mathrm{FV}}_m = \frac{1}{|S^c_m|}\sum_{S^v_p\in\mathcal{V}^c_m}\ell_{mp}\begin{pmatrix}0\\ \frac{g}{2}\left(\overline{\eta}^c_m - \check{\overline{\eta}}^c_m\right)\left(\overline{b}^c_m - \check{\overline{b}}^c_m\right)\mathbf{n}_{mp}\end{pmatrix}.$$

Numerical investigations do not show noticeable variations on the studied test-cases.

4. Fitting the blended fluxes

We are left with the definition of some blending coefficients, which aim at ensuring that the required properties on the resulting approximate solution are strictly enforced, while preserving the highest possible level of accuracy and convergence rate of the scheme. To achieve this, the idea introduced in [75] is to locally reformulate the

monolithic scheme (20) as a Godunov-like scheme at subcells interfaces, and we follow these lines, but accounting for the particularity of the NSW equations.
In what follows, the novel discrete form and the subsequent analysis are developed relying on semi-discrete formulations, together with an extension to fully-discrete case with the first-order Euler time-marching algorithm (various higher-order Runge-Kutta time-marching methods may be used to achieve better convergence in time, and these multistage methods are convex combinations of first-order forward Euler steps).

4.1. Intermediate Riemann states and blending coefficients smoother

As $\sum_{S_p^v\in\mathcal{V}_m^c}\ell_{mp}\mathbf{n}_{mp}=\mathbf{0}$, we have:

$$\begin{aligned}\overline{\mathbf{v}}_m^{c,n+1} &= \overline{\mathbf{v}}_m^{c,n} - \frac{\Delta t^n}{|S_m^c|}\sum_{S_p^v\in\mathcal{V}_m^c}\ell_{mp}\widetilde{\mathbb{F}}_{mp} + \Delta t^n\overline{\mathbf{B}}_m^{c,n} + \frac{\Delta t^n}{|S_m^c|}\mathbb{F}\left(\overline{\mathbf{v}}_m^{c,n},\overline{b}_m^c\right)\cdot\sum_{S_p^v\in\mathcal{V}_m^c}\ell_{mp}\mathbf{n}_{mp} \pm \frac{\sigma\Delta t^n}{|S_m^c|}\sum_{S_p^v\in\mathcal{V}_m^c}\ell_{mp}\overline{\mathbf{v}}_m^{c,n}\\ &= \left(1-\frac{\sigma\Delta t^n}{|S_m^c|}\sum_{S_p^v\in\mathcal{V}_m^c}\ell_{mp}\right)\overline{\mathbf{v}}_m^{c,n} + \frac{\sigma\Delta t^n}{|S_m^c|}\sum_{S_p^v\in\mathcal{V}_m^c}\ell_{mp}\left(\overline{\mathbf{v}}_m^{c,n} - \frac{\widetilde{\mathbb{F}}_{mp}-\mathbb{F}\left(\overline{\mathbf{v}}_m^{c,n},\overline{b}_m^c\right)\cdot\mathbf{n}_{mp}}{\sigma}\right) + \Delta t^n\overline{\mathbf{B}}_m^{c,n}.\end{aligned}$$

Defining the *interior blended Riemann intermediate states* $\widetilde{\mathbf{v}}_{mp}^* := \overline{\mathbf{v}}_m^{c,n} - \frac{\widetilde{\mathbb{F}}_{mp}-\mathbb{F}\left(\overline{\mathbf{v}}_m^{c,n},\overline{b}_m^c\right)\cdot\mathbf{n}_{mp}}{\sigma}$, the previous expression can be recast into the following form

$$\overline{\mathbf{v}}_m^{c,n+1} = \left(1-\frac{\sigma\Delta t^n}{|S_m^c|}\sum_{S_p^v\in\mathcal{V}_m^c}\ell_{mp}\right)\overline{\mathbf{v}}_m^{c,n} + \frac{\sigma\Delta t^n}{|S_m^c|}\sum_{S_p^v\in\mathcal{V}_m^c}\ell_{mp}\widetilde{\mathbf{v}}_{mp}^* + \Delta t^n\overline{\mathbf{B}}_m^{c,n}.$$

The sum parts of this formulation of $\overline{\mathbf{v}}_m^{c,n+1}$ is a convex combination of solution-states, provided that the time step is computed under the CFL condition (4). By means of LF flux definition, we may rewrite the interior blended Riemann intermediate state as

$$\widetilde{\mathbf{v}}_{mp}^* = \frac{\overline{\mathbf{v}}_m^{c,n}+\overline{\mathbf{v}}_p^{v,n}}{2} - \frac{\left(\mathbb{F}\left(\overline{\mathbf{v}}_m^{c,n},\overline{b}_m^c\right)-\mathbb{F}\left(\overline{\mathbf{v}}_p^{v,n},\overline{b}_p^v\right)\right)\cdot\mathbf{n}_{mp}}{2\sigma} - \Theta_{mp}\frac{\Delta\mathbb{F}_{mp}}{\sigma} = \mathbf{v}_{mp}^* - \Theta_{mp}\frac{\Delta\mathbb{F}_{mp}}{\sigma},$$

where $\mathbf{v}_{mp}^*$ is the interior first-order FV Riemann intermediate state. Since the proposed numerical construction relies on non-conservative numerical fluxes (17), we need interior and exterior trace-values for the numerical fluxes, and we have the following definitions of blended Riemann intermediate states:

$$\widetilde{\mathbf{v}}_{mp}^* := \mathbf{v}_{mp}^* - \Theta_{mp}\left(\frac{\widehat{\mathbb{F}}_{mp}-\mathbb{F}_{mp}^{*,\mathrm{FV}}}{\sigma}\right),\qquad \widetilde{\mathbf{v}}_{pm}^* := \mathbf{v}_{pm}^* + \Theta_{mp}\left(\frac{\widehat{\mathbb{F}}_{pm}-\mathbb{F}_{pm}^{*,\mathrm{FV}}}{\sigma}\right),$$

where $\mathbf{v}_{mp}^{*,\pm}$ are the FV intermediate states defined as

$$\mathbf{v}_{mp}^* := \overline{\mathbf{v}}_m^c - \frac{\mathbb{F}_{mp}^{*,\mathrm{FV}}-\mathbb{F}\left(\overline{\mathbf{v}}_m^{c,n},\overline{b}_m^c\right)\cdot\mathbf{n}_{mp}}{\sigma},\qquad \mathbf{v}_{pm}^* := \overline{\mathbf{v}}_m^c - \frac{\mathbb{F}_{pm}^{*,\mathrm{FV}}-\mathbb{F}\left(\overline{\mathbf{v}}_p^{v,n},\overline{b}_p^v\right)\cdot\mathbf{n}_{pm}}{\sigma}.$$

As a consequence, if the numerical initial-data does lie in $\mathscr{H}_b^+$, we show in the following that it is possible to define local blending coefficients Θ_{mp} which allows to reach optimal convergence order in smooth areas, while ensuring that $\overline{\mathbf{v}}_m^c$ remains in $\mathscr{H}_b^+$ during the time-evolution (provided, as usual, that the first-order underlying FV scheme satisfies the positivity property), preventing in the meantime from spurious oscillations in the vicinity of classical shocks, and which is entirely compatible with the preservation of motionless steady-states.

Before describing the detailed construction of such blending coefficients, let us emphasize that it has been previously noted in [75, 76] that, for some particularly non-linear evolutions, a sharp switching between a first-order scheme and a fully high-order scheme can lead to unphysical oscillatory behaviors. For instance, some subcells may be assigned first-order FV fluxes on certain faces (hence $\Theta_{mp}=0$) and fully high-order reconstructed fluxes (hence $\Theta_{mp}=1$) on others. To mitigate such sharp variations, a *blending coefficient smoother* may be introduced and each subcell $S_m^c\in\mathcal{T}_c^{\mathrm{sub}}$ is assigned a blending coefficient Θ_m^c, defined as the average of the blending coefficients of its faces, as follows:

$$\Theta_m^c = \frac{1}{\#\mathcal{V}_m^c}\sum_{S_p^v\in\mathcal{V}_m^c}\Theta_{mp}.$$

Subsequently, *a unique blending coefficient* for each subcell face may be locally adjusted by reducing it to the average of the blending coefficients of all subcells sharing a node with the face Γ_{mp} as follows:

$$\widetilde{\Theta}_{mp} = \min\left(\Theta_{mp}, \frac{1}{\#\mathscr{V}_{mp}} \sum_{S_q^v \in \mathscr{V}_{mp}} \Theta_q^v\right). \tag{21}$$

This is used to produce the numerical results of section 5.

4.2. Water-height positivity (PAD criterium)

It is essential to ensure the positivity of the discrete water-height, which is notoriously challenging for high-order methods. First, let study the first-order FV Riemann intermediate states: for a subcell $S_m^c \in \mathscr{T}_c^{\text{sub}}$ and its neighboring subcell $S_p^v \in \mathscr{V}_m^c$, we show that $\eta_{mp}^* \geq \overline{b}_m^c$ and $\eta_{pm}^* \geq \overline{b}_p^v$.

Proposition 4.1. *The water-height positivity is ensured on first-order FV Riemann intermediate states for the subcell FV fluxes.*

Proof. We just need to ensure that for all $\omega_c \in \mathscr{T}_h$, for all $S_m^c \in \mathscr{T}_c^{\text{sub}}$, $\overline{\eta}_m^{c,n} \geq \overline{b}_m^{c,n}$. Dropping the superscript n and using the notation $\mathbb{F}_{mp}^{*,\eta}$ for the first component of the numerical FV flux $\mathbb{F}_{mp}^{*,\text{FV}}$, we only need to verify is that for any $S_m^c \in \mathscr{T}_c^{\text{sub}}$, we have

$$\eta_{mp}^* = \overline{\eta}_m^c - \frac{\mathbb{F}_{mp}^{*,\eta} - \overline{\mathbf{q}}_m^c \cdot \mathbf{n}_{mp}}{\sigma} \geq \overline{b}_m^c, \quad \text{and} \quad \eta_{pm}^* = \overline{\eta}_p^v - \frac{\mathbb{F}_{pm}^{*,\eta} - \overline{\mathbf{q}}_p^v \cdot \mathbf{n}_{mp}}{\sigma} \geq \overline{b}_p^v.$$

Noticing that $\check{\overline{\eta}}_p^v - \check{\overline{\eta}}_m^c = \check{\overline{H}}_p^v - \check{\overline{H}}_m^c + \check{\overline{b}}_{mp} - \check{\overline{b}}_{mp} = \check{\overline{H}}_p^v - \check{\overline{H}}_m^c$, and using the velocity notation $\overline{\mathbf{u}}_m^c := \frac{\overline{\mathbf{q}}_m^c}{\overline{H}_m^c}$, we have

$$\begin{aligned}
\eta_{mp}^* = \overline{\eta}_m^c - \frac{\mathbb{F}_{mp}^{*,\eta} - \overline{\mathbf{q}}_m^c \cdot \mathbf{n}_{mp}}{\sigma} &= \overline{H}_m^c + \overline{b}_m^c - \frac{\mathbb{F}_{mp}^{*,\eta} - \overline{\mathbf{q}}_m^c \cdot \mathbf{n}_{mp}}{\sigma} \\
&= \frac{1}{2}\left(2\overline{H}_m^c + \check{\overline{H}}_p^v - \check{\overline{H}}_m^c\right) - \frac{1}{2\sigma}\left(\check{\overline{\mathbf{q}}}_p^v - \check{\overline{\mathbf{q}}}_m^c - 2\overline{\mathbf{q}}_m^c\right) \cdot \mathbf{n}_{mp} + \overline{b}_m^c \\
&= \frac{1}{2}\left(2\overline{H}_m^c + \check{\overline{H}}_p^v - \check{\overline{H}}_m^c\right) - \frac{1}{2\sigma}\left(\check{\overline{H}}_p^v\overline{\mathbf{u}}_m^c - \check{\overline{H}}_m^c\overline{\mathbf{u}}_m^c - 2\overline{H}_m^c\overline{\mathbf{u}}_m^c\right) \cdot \mathbf{n}_{mp} + \overline{b}_m^c.
\end{aligned}$$

Writing it this way demonstrate that we just need to have

$$\frac{1}{2}\left(2\overline{H}_m^c + \check{\overline{H}}_p^v - \check{\overline{H}}_m^c\right) - \frac{1}{2\sigma}\left(\check{\overline{H}}_p^v\overline{\mathbf{u}}_m^c - \check{\overline{H}}_m^c\overline{\mathbf{u}}_m^c - 2\overline{H}_m^c\overline{\mathbf{u}}_m^c\right) \cdot \mathbf{n}_{mp} \geq 0.$$

By construction, we easily have $0 \leq \check{\overline{H}}_m^c \leq \overline{H}_m^c$ and $0 \leq \check{\overline{H}}_p^v \leq \overline{H}_p^v$, so we easily get $2\overline{H}_m^c + \check{\overline{H}}_p^v - \check{\overline{H}}_m^c \geq 2\overline{H}_m^c$. For the other term, let us rearrange it into

$$\left(\check{\overline{H}}_p^v\overline{\mathbf{u}}_m^c - \check{\overline{H}}_m^c\overline{\mathbf{u}}_m^c - 2\overline{H}_m^c\overline{\mathbf{u}}_m^c\right) \cdot \mathbf{n}_{mp} = \left(\left(2\overline{H}_m^c - \check{\overline{H}}_m^c\right)\frac{1 + \overline{\mathbf{u}}_m^c\sigma^{-1}}{2} + \check{\overline{H}}_p^v \frac{1 + \overline{\mathbf{u}}_p^v\sigma^{-1}}{2}\right) \cdot \mathbf{n}_{mp},$$

and according to CFL (4) and hydrostatic reconstructions, we get:

$$2\overline{H}_m^c - \check{\overline{H}}_m^c \geq \overline{H}_m^c, \qquad \left(\frac{1 + \overline{\mathbf{u}}_m^c\sigma^{-1}}{2}\right) \cdot \mathbf{n}_{mp} \geq 0, \qquad \check{\overline{H}}_p^v \geq 0, \qquad \left(\frac{1 + \overline{\mathbf{u}}_p^v\sigma^{-1}}{2}\right) \cdot \mathbf{n}_{mp} \geq 0.$$

This leads to $\eta_{mp}^* \geq \overline{b}_m^c$ and, in the same way, we show that $\eta_{pm}^* \geq \overline{b}_p^v$. ☐

We are able to find a blending coefficient $\Theta_{mp}^{\mathscr{H}^+}$ that ensures preservation of water-height positivity:

Proposition 4.2. *Under the CFL condition (4), if for all $\omega_c \in \mathscr{T}_h$, for all $S_m^c \in \mathscr{T}_c^{\text{sub}}$, $\overline{\mathbf{v}}_m^{c,n} \in \mathscr{H}^+$, then for all $\omega_c \in \mathscr{T}_h$, for all $S_m^c \in \mathscr{T}_c^{\text{sub}}$, $\overline{\mathbf{v}}_m^{c,n+1} \in \mathscr{H}^+$, provided that the blending coefficient $\Theta_{mp}^{\mathscr{H}^+}$, satisfies*

$$\Theta_{mp}^{\mathscr{H}^+} \leq \min\left(\Theta_{mp}^{\mathscr{H}^+,-}, \Theta_{mp}^{\mathscr{H}^+,+}\right),$$

with

$$\Theta_{mp}^{\mathscr{H}^+,-} \leq \begin{cases} \dfrac{\sigma\left(\eta^*_{mp} - \overline{b}^c_m\right)}{\Delta\mathbb{F}_{mp}} & \textit{if } \Delta\mathbb{F}_{mp} > 0, \\ 1 & \textit{else,} \end{cases} \qquad \Theta_{mp}^{\mathscr{H}^+,+} \leq \begin{cases} \dfrac{\sigma\left(\overline{b}^v_p - \eta^*_{pm}\right)}{\Delta\mathbb{F}_{pm}} & \textit{if } \Delta\mathbb{F}_{pm} < 0, \\ 1 & \textit{else,} \end{cases}$$

with the notation $\Delta\mathbb{F}_{mp} := \widehat{\mathbb{F}}_{mp} - \mathbb{F}^{*,\mathrm{FV}}_{mp}$.

Remark 4.3. *We emphasize that a neat computation of the discrete initial-data is required, to ensure the initial positivity of the water-height both at the cells and subcells scales. To achieve this, we first compute the subcell mean-values of the variables and then apply the projection matrix* $\mathbb{P}_c$ *to recover the cell polynomial representation, ensuring that the approximate initial-data belongs to* $\mathscr{H}_b^+$ *(or, more generally, to any convex set of admissible states of interest). Indeed, the approximate initial data* $\mathbf{v}_h^0$ *must be admissible in order to generate a sequence of admissible states under the CFL condition and the chosen blending coefficients. Starting from a physical or idealized (analytical) initial-data* $\mathbf{v}^0 := (\eta^0, q_x^0, q_y^0)$ *and a bathymetry parameterization* b *such that* $\eta^0 - b \geq 0$, *we observe that* $\widetilde{\pi}_h^k(\eta^0 - b) \geq 0$. *Therefore, the subcell representation* $\overline{\mathbf{v}}_h^0 := \widetilde{\pi}_h^k \mathbf{v}^0$ *is admissible. In the same spirit, we also have that* $\mathbf{v}_h^0 := (\overline{\pi}_h^k)^{-1}\overline{\mathbf{v}}_h^0$ *remains admissible. From this last relation, we see that the approximate initial surface elevation must be defined consistently with the previous definition of the approximate bathymetry:*

$$\eta_h^0 := (\overline{\pi}_h^k)^{-1}\widetilde{\pi}_h^k\eta^0 - b_h. \tag{22}$$

4.3. Relaxed subcell numerical admissibility detection (SubNAD criterium)

To prevent unphysical oscillations in the vicinity of discontinuities, we mimic a local maximum principle, on the sub-mean values, by enforcing the sub-mean elevation $\overline{\eta}_m^{c,n+1}$ to be bounded by the sub-mean values at the previous time step (or previous RK step in time integration) in a given subcell set, as follows:

$$\alpha_m^c := \min_{S_p^v \in \mathcal{N}(S_m^c)} \overline{\eta}_p^{v,n} \leq \overline{\eta}_m^{c,n+1} \leq \max_{S_p^v \in \mathcal{N}(S_m^c)} \overline{\eta}_p^{v,n} =: \beta_m^c, \tag{23}$$

Proposition 4.4. *To ensure condition (23) is satisfied for any subcell, it is sufficient to verify that* $\widetilde{\eta}^{*,-}_{mp} \in [\alpha^c_m, \beta^c_m]$ *and* $\widetilde{\eta}^{*,+}_{mp} \in [\alpha^v_p, \beta^v_p]$. *Since* $\eta^{*,\pm}_{mp}$ *satisfies both conditions, it suffices to impose the following constraint on* Θ_{mp}*:*

$$\Theta_{mp}^{\mathrm{SubNAD}} \leq \min\left(1, \left|\frac{\sigma}{\Delta\mathbb{F}_{mp}}\right| \begin{cases} \min\left(\beta^v_p - \eta^{*,+}_{mp},\ \eta^{*,-}_{mp} - \alpha^c_m\right) & \textit{if } \Delta\mathbb{F}_{mp} > 0, \\ \min\left(\beta^c_m - \eta^{*,-}_{mp},\ \eta^{*,+}_{mp} - \alpha^v_p\right) & \textit{if } \Delta\mathbb{F}_{mp} < 0. \end{cases}\right).$$

As in [75, 76], we also introduce some relaxation through a smooth extrema detector in order to preserve the scheme's accuracy in the presence of smooth extrema. This detector is based on the smoothness indicator for finite elements, as described in [45]. The main idea is as follows: the numerical solution is considered to exhibit a smooth extrema profile if the linearized version of the numerical solution's spatial derivatives represents a monotonous profile. To achieve this, we introduce the following subcell linear reconstructions:

$$\mathfrak{E}_x^m(\boldsymbol{x}) = \overline{\partial_x \eta_h^c}^m + \overline{\nabla_{\boldsymbol{x}}(\partial_x \eta_h^c)}^m \cdot (\boldsymbol{x} - \boldsymbol{x}_m^c), \tag{24}$$

$$\mathfrak{E}_y^m(\boldsymbol{x}) = \overline{\partial_y \eta_h^c}^m + \overline{\nabla_{\boldsymbol{x}}(\partial_y \eta_h^c)}^m \cdot (\boldsymbol{x} - \boldsymbol{x}_m^c). \tag{25}$$

In the above, $\boldsymbol{x}_m^c$ represents the barycenter of the subcell S_m^c, and $\overline{\partial_{x\backslash y}\eta_h^c}^m$ and $\overline{\nabla_{\boldsymbol{x}}(\partial_{x\backslash y}\eta_h^c)}^m$ denote the subcell averages of the successive partial derivatives of η_h^c. The smoothness indicator functions $\mathfrak{E}_x^m$ and $\mathfrak{E}_y^m$, being linear, attain their extrema at the vertices $\boldsymbol{x}_q \in \mathscr{P}_m^c$. To confirm that the numerical solution η_h presents a smooth profile within subcell S_m^c, we require that the linearized spatial derivative functions satisfy the following constraints:

$$\mathfrak{E}_{x,q}^{\min} \leq \mathfrak{E}_x^m(\boldsymbol{x}_q) \leq \mathfrak{E}_{x,q}^{\max} \quad \text{and} \quad \mathfrak{E}_{y,q}^{\min} \leq \mathfrak{E}_y^m(\boldsymbol{x}_q) \leq \mathfrak{E}_{y,q}^{\max}, \tag{26}$$

where $\mathfrak{E}_{x\backslash y,q}^{\min}$ and $\mathfrak{E}_{x\backslash y,q}^{\max}$ are defined as:

$$\mathfrak{E}_{x\backslash y,q}^{\min} = \min_{S_m^c \in \mathscr{V}_q} \mathfrak{E}_{x\backslash y}^m(\boldsymbol{x}_q) \quad \text{and} \quad \mathfrak{E}_{x\backslash y,q}^{\max} = \max_{S_m^c \in \mathscr{V}_q} \mathfrak{E}_{x\backslash y}^m(\boldsymbol{x}_q).$$

In practice, if condition (26) holds for all vertices $x_q \in \mathscr{P}_m^c$, the numerical solution η_h can be regarded as smooth within subcell S_m^c. Additionally, if the solution is smooth in both subcells S_m^c and S_p^v, the blending coefficient constraint through the discrete local maximum condition (23) can be relaxed (ie. $\Theta_{mp} = 1$).

Remark 4.5. *Smooth extrema detection is not required for second-order approximations. For third-order local subcell monolithic DG/FV schemes, however, the smoothness detector must operate at the cell level. Indeed, in this case, the second derivatives* $\nabla_{\boldsymbol{x}}(\partial_{x\setminus y}\eta_h^c)$ *are constant and do not require additional subcell-level computations.*

4.4. Well-Balancing for motionless steady-states

In this section, we show that the previous constrained choices of blended coefficients, when combined together with local and global hydrostatic-like reconstructions, do allow to preserve a well-balanced property.

Remark 4.6. *Let us note that under the motionless steady-state assumption* $\eta_h = \eta^e > 0$ *and* $\mathbf{q}_h^n = \mathbf{0}$*, the following relation holds:*

$$\nabla_{\boldsymbol{x}} \cdot \mathbb{F}(\mathbf{v}_c, b_c) = \mathbf{B}[b_c](\mathbf{v}_c), \qquad \forall \omega_c \in \mathscr{T}_h.$$

Moreover, as we have

$$\mathbb{F}(\mathbf{v}_h, b_h) = \begin{pmatrix} 0 & 0 \\ \frac{1}{2}g\left(\eta_h^2 - 2\eta_h b_h\right) & 0 \\ 0 & \frac{1}{2}g\left(\eta_h^2 - 2\eta_h b_h\right) \end{pmatrix},$$

we emphasize that $\mathbb{F}(\mathbf{v}_h, b_h)$ *belongs to* $\mathscr{M}_{2\times 3}\left(\mathbb{P}^{2k}(\mathscr{T}_h)\right)$*. Therefore at steady state,*

$$\mathbb{F}_h := p^k_{\mathscr{T}_h} \circ \mathbb{F}(\mathbf{v}_h, b_h) = \mathbb{F}(\mathbf{v}_h, b_h).$$

Proposition 4.7. *The discrete formulation* (20) *preserves the motionless steady states, provided that the integrals in both the DG and FV subcell formulations are exactly computed at steady-states. We then have:*

$$\forall n \in \mathbb{N}, \quad \forall \eta^e \in \mathbb{R}, \qquad \left(\eta_h^n = \eta^e \text{ and } \mathbf{q}_h^n = \mathbf{0}\right) \Longrightarrow \left(\eta_h^{n+1} = \eta^e \text{ and } \mathbf{q}_h^{n+1} = \mathbf{0}\right).$$

Proof. Let us recall that the discrete formulation of the monolithic DG/FV subcell scheme is given by:

$$\overline{\mathbf{v}}_m^{c,n+1} = \overline{\mathbf{v}}_m^{c,n} - \frac{\Delta t^n}{|S_m^c|} \sum_{S_p^v \in \mathscr{V}_m^c} \ell_{mp} \widetilde{\mathbb{F}}_{mp} + \Delta t^n \overline{\mathbf{B}}_m^{c,n}.$$

At motionless steady state, we want to show that the numerical fluxes are cancelling the source term,

$$\frac{1}{|S_m^c|} \sum_{S_p^v \in \mathscr{V}_m^c} \ell_{mp} \widetilde{\mathbb{F}}_{mp} = \overline{\mathbf{B}}_m^{c,n} \qquad \text{s.t.} \qquad \overline{\mathbf{v}}_m^{c,n+1} = \overline{\mathbf{v}}_m^{c,n}. \tag{27}$$

Since the blended flux $\widetilde{\mathbb{F}}_{mp}$ is a convex combination of the first-order FV flux $\mathbb{F}_{mp}^{*,\text{FV}}$ and the high-order reconstructed flux $\widehat{\mathbb{F}}_{mp}$, it is enough to prove that the source term is exactly cancelled by both fluxes. Let us first consider the case where the blending Θ is set to 1, meaning we consider only the high-order contribution. We have

$$\widehat{\mathbb{F}}_c = \begin{cases} \mathbb{F}_c - \mathbb{A}_c^\top \mathscr{L}_c^{-1} \partial \mathbb{F}_c & \text{in } \omega_c \setminus \overline{\partial \omega_c}, \\ \mathbb{F}^{*,\text{DG}}_{\partial\omega_c} & \text{on } \partial\omega_c, \end{cases}$$

where

$$(\partial \mathbb{F}_c)_m = \int_{\partial \omega_c} \left(\mathbb{F}_h^c \cdot \mathbf{n}_{\partial\omega_c} - \mathbb{F}^{*,\text{DG}}_{\partial\omega_c}\right) \widetilde{\phi}_m^c(s)\, \mathrm{d}s.$$

Let us show that, under steady-states assumption, for each interface $\Gamma_{cv(k)} \subset \partial\omega_c$, $k \in [\![1, \#\mathscr{F}_c]\!]$, we have $\mathbb{F}^{*,\text{DG}}_{cv(k)} = \mathbb{F}_h^c \cdot \mathbf{n}_{cv(k)}$. This can simply be obtained by remarking that

$$\mathbb{F}_h^c \cdot \mathbf{n}_{cv(k)} = \mathbb{F}(\mathbf{v}_k^-, b_k^-) \cdot \mathbf{n}_{cv(k)} = \mathbb{F}\left(\begin{pmatrix} \eta^e \\ \mathbf{0} \end{pmatrix}, b_k^-\right) \cdot \mathbf{n}_{cv(k)} = \begin{pmatrix} 0 & 0 \\ \frac{1}{2}g\left((\eta^e)^2 - 2\eta^e b_k^-\right) & 0 \\ 0 & \frac{1}{2}g\left((\eta^e)^2 - 2\eta^e b_k^-\right) \end{pmatrix} \cdot \mathbf{n}_{cv(k)}$$

and also

$$
\begin{aligned}
\mathbb{F}^{*,\text{DG}}_{cv(k)} &= \frac{\mathbb{F}(\check{\mathbf{v}}_k^-, \check{b}_k) + \mathbb{F}(\check{\mathbf{v}}_k^+, \check{b}_k)}{2} \cdot \mathbf{n}_{cv(k)} - \frac{\sigma}{2}\left(\check{\mathbf{v}}_k^+ - \check{\mathbf{v}}_k^-\right) + \check{\mathbb{F}}_{cv(k)} = \frac{\mathbb{F}(\check{\mathbf{v}}_k^-, \check{b}_k) + \mathbb{F}(\check{\mathbf{v}}_k^+, \check{b}_k)}{2} \cdot \mathbf{n}_{cv(k)} + \check{\mathbb{F}}_{cv(k)} \\
&= \left\{ \begin{pmatrix} 0 & 0 \\ \frac{1}{2} g \left((\eta^e)^2 - 2\eta^e \check{b}_k \right) & 0 \\ 0 & \frac{1}{2} g \left((\eta^e)^2 - 2\eta^e \check{b}_k \right) \end{pmatrix} + \begin{pmatrix} 0 & 0 \\ \mathrm{g}\eta^e (\check{b}_k - b_k^-) & 0 \\ 0 & \mathrm{g}\eta^e (\check{b}_k - b_k^-) \end{pmatrix} \right\} \cdot \mathbf{n}_{cv(k)} \\
&= \begin{pmatrix} 0 & 0 \\ \frac{1}{2} g \left((\eta^e)^2 - 2\eta^e b_k^- \right) & 0 \\ 0 & \frac{1}{2} g \left((\eta^e)^2 - 2\eta^e b_k^- \right) \end{pmatrix} \cdot \mathbf{n}_{cv(k)}.
\end{aligned}
$$

This means that we have

$$
\widehat{\mathbb{F}}_c = \begin{cases} \mathbb{F}_c & \text{in } \omega_c \setminus \overline{\partial \omega_c}, \\ \mathbb{F}^{*,\text{DG}}_{\partial \omega_c} & \text{on } \partial \omega_c, \end{cases}
$$

and therefore, by Remark 4.6, we have $\widehat{\mathbb{F}}_c = \mathbb{F}(\mathbf{v}_h^c, b_h^c)$ at steady states and we can write:

$$
\sum_{S_p^v \in \mathscr{V}_m^c} \ell_{mp} \widehat{\mathbb{F}}_{mp} = \int_{S_m^c} \nabla_{\boldsymbol{x}} \cdot \mathbb{F}_h^c \, \mathrm{d}\boldsymbol{x} = \int_{S_m^c} \nabla_{\boldsymbol{x}} \cdot \mathbb{F}(\mathbf{v}_h^c, b_h^c) \, \mathrm{d}\boldsymbol{x}.
$$

We get then

$$
\frac{1}{|S_m^c|} \sum_{S_p^v \in \mathscr{V}_m^c} \ell_{mp} \widehat{\mathbb{F}}_{mp} - \overline{\mathbf{B}}_m^{c,n} = \frac{1}{|S_m^c|} \left(\int_{S_m^c} \nabla_{\boldsymbol{x}} \cdot \mathbb{F}(\mathbf{v}_h^c, b_h^c) \, \mathrm{d}\boldsymbol{x} - \int_{S_m^c} \mathbf{B}(\mathbf{v}_h^c, \nabla_{\boldsymbol{x}} b_h^c) \, \mathrm{d}\boldsymbol{x} \right),
$$

and since we have $\nabla_{\boldsymbol{x}} \cdot \mathbb{F}(\mathbf{v}_h^c, b_h^c) = \mathbf{B}(\mathbf{v}_h^c, \nabla_{\boldsymbol{x}} b_h^c)$ at steady states,

$$
\frac{1}{|S_m^c|} \sum_{S_p^v \in \mathscr{V}_m^c} \ell_{mp} \widehat{\mathbb{F}}_{mp} - \overline{\mathbf{B}}_m^{c,n} = 0 \qquad \text{s.t.} \qquad \overline{\mathbf{v}}_m^{c,n+1} = \overline{\mathbf{v}}_m^{c,n}.
$$

Let us now consider $\Theta = 0$, meaning that we consider only the first-order FV flux contributions, we show that

$$
\frac{1}{|S_m^c|} \sum_{S_p^v \in \mathscr{V}_m^c} \ell_{mp} \mathbb{F}^{*,\text{FV}}_{mp} = \overline{\mathbf{B}}_m^{c,n} \qquad \text{s.t.} \qquad \overline{\mathbf{v}}_m^{c,n+1} = \overline{\mathbf{v}}_m^{c,n}.
$$

Let us note that

$$
\begin{aligned}
\mathbb{F}^{*,\text{FV}}_{mp} &= \frac{\mathbb{F}(\check{\overline{\mathbf{v}}}_m^c, \check{\overline{b}}_{mp}) + \mathbb{F}(\check{\overline{\mathbf{v}}}_p^v, \check{\overline{b}}_{mp})}{2} \cdot \mathbf{n}_{mp} - \frac{\sigma}{2}\left(\check{\overline{\mathbf{v}}}_p^v - \check{\overline{\mathbf{v}}}_m^c\right) + \check{\mathbb{F}}^{\text{FV}}_{mp} = \frac{\mathbb{F}(\check{\overline{\mathbf{v}}}_m^c, \check{\overline{b}}_{mp}) + \mathbb{F}(\check{\overline{\mathbf{v}}}_p^v, \check{\overline{b}}_{mp})}{2} \cdot \mathbf{n}_{mp} + \check{\mathbb{F}}^{\text{FV}}_{mp} \\
&= \left\{ \begin{pmatrix} 0 & 0 \\ \frac{1}{2} g \left((\eta^e)^2 - 2\eta^e \check{\overline{b}}_{mp} \right) & 0 \\ 0 & \frac{1}{2} g \left((\eta^e)^2 - 2\eta^e \check{\overline{b}}_{mp} \right) \end{pmatrix} + \begin{pmatrix} 0 & 0 \\ \mathrm{g}\eta^e \left(\check{\overline{b}}_{mp} - b_{mp} \right) & 0 \\ 0 & \mathrm{g}\eta^e \left(\check{\overline{b}}_{mp} - b_{mp} \right) \end{pmatrix} \right\} \cdot \mathbf{n}_{mp} \\
&= \begin{pmatrix} 0 & 0 \\ \frac{1}{2} g \left((\eta^e)^2 - 2\eta^e b_{mp} \right) & 0 \\ 0 & \frac{1}{2} g \left((\eta^e)^2 - 2\eta^e b_{mp} \right) \end{pmatrix} \cdot \mathbf{n}_{mp}.
\end{aligned}
$$

Since $b_{mp} := \frac{1}{|S_m^c|} \int_{\Gamma_{mp}^c} b_h^c(s) \, \mathrm{d}s$, it indeed implies equality between the numerical flux $\mathbb{F}^{*,\text{FV}}_{mp}$ and the flux function $\mathbb{F}_h^c \cdot \mathbf{n}_{mp}$ at steady-states. For any interface Γ_{mp} and in the general case $\Theta_{mp} \in [0,1]$ we have for all $S_m^c \in \mathscr{T}_c^{\text{sub}}$, for all $S_p^v \in \mathscr{V}_m^c$, $\widehat{\mathbb{F}}_{mp} = \mathbb{F}^{*,\text{FV}}_{mp} = \mathbb{F}_h^c \cdot \mathbf{n}_{mp}$ at steady-states, and we easily get the following:

$$
\begin{aligned}
\frac{1}{|S_m^c|} \sum_{S_p^v \in \mathscr{V}_m^c} \ell_{mp} \widetilde{\mathbb{F}}_{mp} &= \frac{1}{|S_m^c|} \sum_{S_p^v \in \mathscr{V}_m^c} \ell_{mp} \mathbb{F}^{*,\text{FV}}_{mp} + \frac{1}{|S_m^c|} \sum_{S_p^v \in \mathscr{V}_m^c} \ell_{mp} \Theta_{mp} \left(\widehat{\mathbb{F}}_{mp} - \mathbb{F}^{*,\text{FV}}_{mp} \right) \\
&= \frac{1}{|S_m^c|} \sum_{S_p^v \in \mathscr{V}_m^c} \ell_{mp} \mathbb{F}^{*,\text{FV}}_{mp} = \overline{\mathbf{B}}_m^{c,n}.
\end{aligned}
$$

□

5. Numerical simulations

In this section, we show that the previous discrete formulation is operational and that the claimed properties are ensured in various existing scenarios, demonstrating that the expected and previously proven properties are effectively observable in a reliable manner. If not stated otherwise, the numerical simulations are produced using the monolithic DG/FV scheme with relaxed SubNAD and PAD criteria, with the blending smoother (21). Both subdivisions are shown (i.e. fully triangular and quadrilateral/triangular one), as neither of them affects the quality of numerical results. When presenting pseudo-1D results (i.e. domain slices and density profiles), we either display the subcell mean values or the cell-averaged values (i.e., the mean of their corresponding subcell values) to ensure that the plots is readable.

5.1. Steady vortex with smooth bathymetry

Simulation parameters.

Computational domain: $\Omega = [-5,5]^2$
Number of cells: $n_{\text{el}} = 200$, 800, 3200, 12800 cells
Boundary conditions: Dirichlet
Polynomial degree: $k = 1,2,3$
Time-marching order: $p = 3$
Final time: $t_{\max} = 1$ sec

This first test-case aim at assessing the convergence properties of the method in some optimal set-up, with the occurence of a smooth bathymetry: we consider a steady vortex configuration detailed in [57]. The bathymetry is $b(\boldsymbol{x}) = 0.2e^{0.5(1-r^2)}$ ($r^2 = x^2+y^2$) and the corresponding exact solution, illustrated in Figure 6, is $\mathbf{v} = (\eta, \mathbf{q})^\top$, is given by:

$$H(\boldsymbol{x},t) = 1 - \frac{1}{4g}e^{2(1-r^2)} - b(\boldsymbol{x}), \qquad \eta(\boldsymbol{x},t) = H(\boldsymbol{x},t) + b(\boldsymbol{x}),$$
$$q_x(\boldsymbol{x},t) = H(\boldsymbol{x},t)\left(ye^{1-r^2}\right), \qquad q_y(\boldsymbol{x},t) = H(\boldsymbol{x},t)\left(-xe^{1-r^2}\right),$$

which allows to quantitatively compare the approximate and expected solutions at a given discrete-time. Even if not fully displayed here for the sake of conciseness, we report some excellent agreements for both conservative variables, and we emphasize that an "optimal" convergence-order of $\mathcal{O}(k+1)$ is observed in every studied computational scenario. As an example, we show color-valued free-surface elevation on Fig. 6 for a particular simulation (similar results are observable with the discharge) and we report the corresponding error-values in Table 7, with practical details of the computation provided in the grey summary-box above. We emphasize that such an optimal behavior is achieved even using the relaxed-SubNAD criterium, ensuring that this particular numerical trick does not modulate the leading error terms, even when considering higher-order approximations.

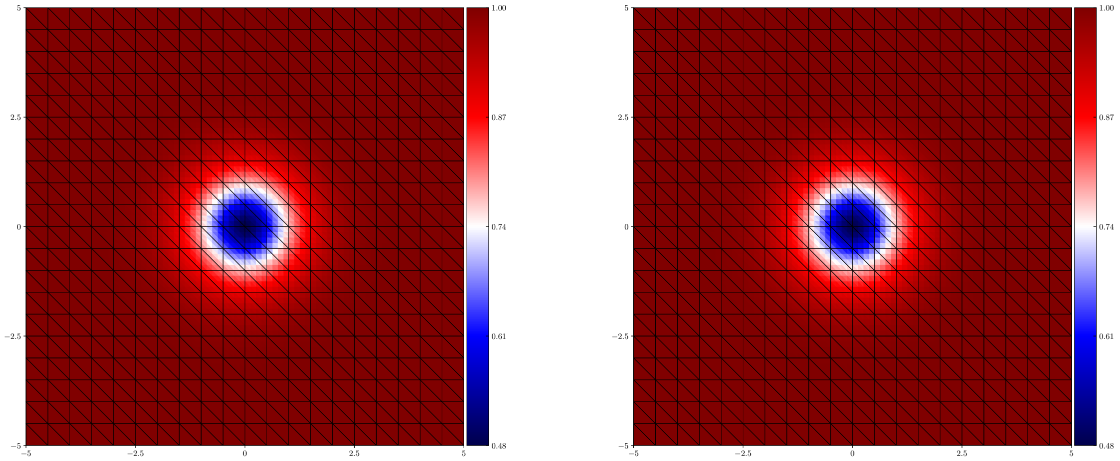

Figure 6: Steady vortex – Exact (left) and $\mathbb{P}^3$ numerical (right) height at final time $t = 1$ sec on 800 cells.

k	1		2		3	
h	$E^{\eta}_{L^2}$	$q^{\eta}_{L^2}$	$E^{\eta}_{L^2}$	$q^{\eta}_{L^2}$	$E^{\eta}_{L^2}$	$q^{\eta}_{L^2}$
1	9.445E-2	2.35	1.529E-2	2.91	4.580E-3	4.19
$\frac{1}{2}$	1.854E-2	2.16	2.039E-3	3.03	2.505E-4	4.10
$\frac{1}{4}$	4.158E-3	2.07	2.491E-4	2.97	1.465E-5	4.00
$\frac{1}{8}$	9.923E-4	–	3.187E-5	–	9.165E-7	–

Figure 7: Steady vortex – L^2-errors between numerical and analytical solutions and convergence rates for η at time $t = 1$ sec.

5.2. Well-balancing

Simulation parameters.

Computational domain: $\Omega = [0, 2] \times [0, 1]$
Number of cells: $n_{\text{el}} = 506, 2064$ cells
Boundary conditions: solid-walls

Polynomial degree: $k = 4$
Time-marching order: $p = 3$
Final time: $t_{\max} = 20$ sec

We perform numerical experiments to assess the well-balancedness of the scheme and we consider a non-uniform topography defined as follows:

$$b(\boldsymbol{x}) = \begin{cases} 0.5e^{-100((x-1.2)^2+150(y-0.7)^2)} & \text{if } x > 0.68, \\ -0.5e^{-100((x-0.45)^2+150(y-0.4)^2)} & \text{otherwise.} \end{cases}$$

Two different set-ups are investigated on unstructured and coarse meshes, in order to assess the capability of our numerical method to preserve motionless balance within a high-order setting: : fully-immerged and partly-immerged bathymetry, see Figures 8–9 for a visual description.

Fully immerged

At $t = 0$, we prescribe $\eta_0 = 1$ and $\mathbf{q}_0 = 0$ and the algorithm preserves this initial-data up to machine-accuracy, with an adaptive time-step that stays strictly constant during all the computation, up to the two last digits (machine accuracy in double-precision). We show on Fig. 8 the corresponding flat free-surface profile, and the associated blending coefficient, which remains stuck to 1 as expected.

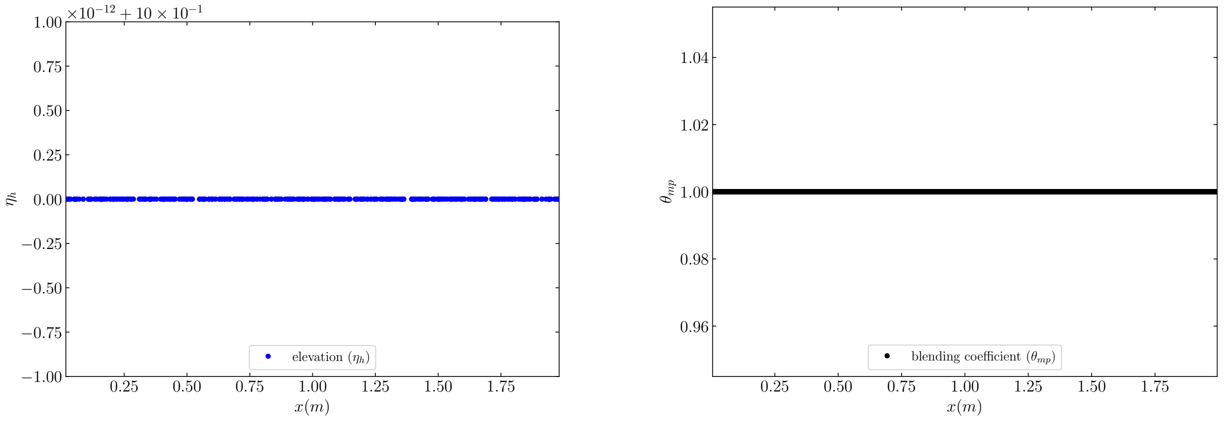

Figure 8: Well-balancing with fully-imerged bathymetry – At $t = 20$ sec: free-surface elevation (left), corresponding blending coefficient (right)

Partly immerged

Going further into the practical investigations, we consider a finer mesh of 2064 cells, and initially prescribe a localized dry area by setting $\eta_0 = \max(b, 0.2)$ and $\mathbf{q}_0 = 0$ (see Fig 9). Previous machine-accuracy preservation may be also obtained provided that a matching mesh, perfectly compatible with the wet/dry contact line, is used. With general (non-matching) meshes, tiny oscillations may be classically observed near the contact-line for the discharge and for higher-order approximations, as expected and exhibited in Figures 10–11. We emphasize that such an issue is inherent to the nature of wet-dry interfaces located *inside* mesh elements, as the same local polynomial approximations have to alternatively approximate, into the same mesh element, free-surface and bathymetry. If such a situation generally generates numerical instabilities for globally high-order methods, it is remarkable to observe that the subcell resolution capability of the new proposed approach, although not perfect, allows to largely mitigate such mesh-geometry disagreement oscillations, as expected from operational and robust methods. These neither propagate nor amplify with respect to time, and from our extensive investigations, they do not affect the global accuracy. Thanks to the PAD, the simulation remains globally stable and the blending coefficients are automatically adapted to properly handle the presence of the dry area, as shown in Fig. 10 within a vertical slice of the computational domain through the bump, while Fig. 11 displays the bathymetry bump/hole locations, together with free-surface elevation, discharge norm, and a map of blending coefficients mean-values per subcell, in order to clearly observe the PAD activation and effective corrections. Importantly, this shows that the correction mechanism is only switched-on in the vicinity of dry areas, as expected, which highlights the robustness and efficiency of the proposed framework in globally optimizing the preservation the full accuracy of the higher-order underlying DG scheme. Note that in both cases, we also run the computations for (very) long times of several physical hours without noticing any sensible error-increasing due to local flux/bathymetry balancing fail.

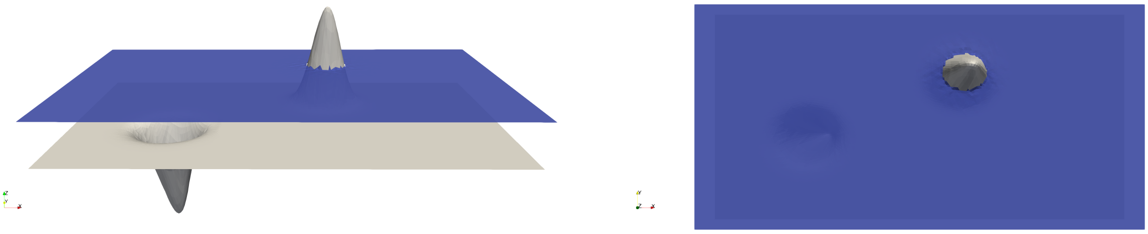

Figure 9: Well-balancing with dry area – Free-surface elevation and topography at $t = 20$ sec.

5.3. Dam-breaks in a channel

In this third test-case, we consider extruded 1D dam-break problems in a channel, inducing a directional propagation (along the x-direction), but using general unstructured meshes without anisotropy, providing a (classical) benchmark to evaluate the ability of the numerical methods to handle strong discontinuities or singularities, together with the preservation of the water-height positivity in the limit cases. We set $b(\boldsymbol{x}) = 0$ and investigate both the wet/wet and wet/dry situations, described in the following.

On a wet-bed

Simulation parameters.

Computational domain: $\Omega = [0, 1000] \times [0, 200]$
Number of cells: $n_{\text{el}} = 350$ cells
Boundary conditions: solid walls
Polynomial degree: $k = 4$
Time-marching order: $p = 3$
Final time: $t_{\max} = 32$ sec

We consider the initial-data

$$\eta(\boldsymbol{x}, 0) = \begin{cases} 10 & \text{if } x < 500, \\ 7 & \text{otherwise,} \end{cases} \qquad \mathbf{q}(\boldsymbol{x}, 0) = \mathbf{0},$$

and use a very coarse mesh of only 350 (unstructured) cells, not aligned with the propagation direction, together with an approximate piecewise-polynomial solution of degree $k = 4$. We emphasize that considering such a mesh-size, the sharp variations of the Riemann solution may be entirely located inside one mesh-element (in the lateral

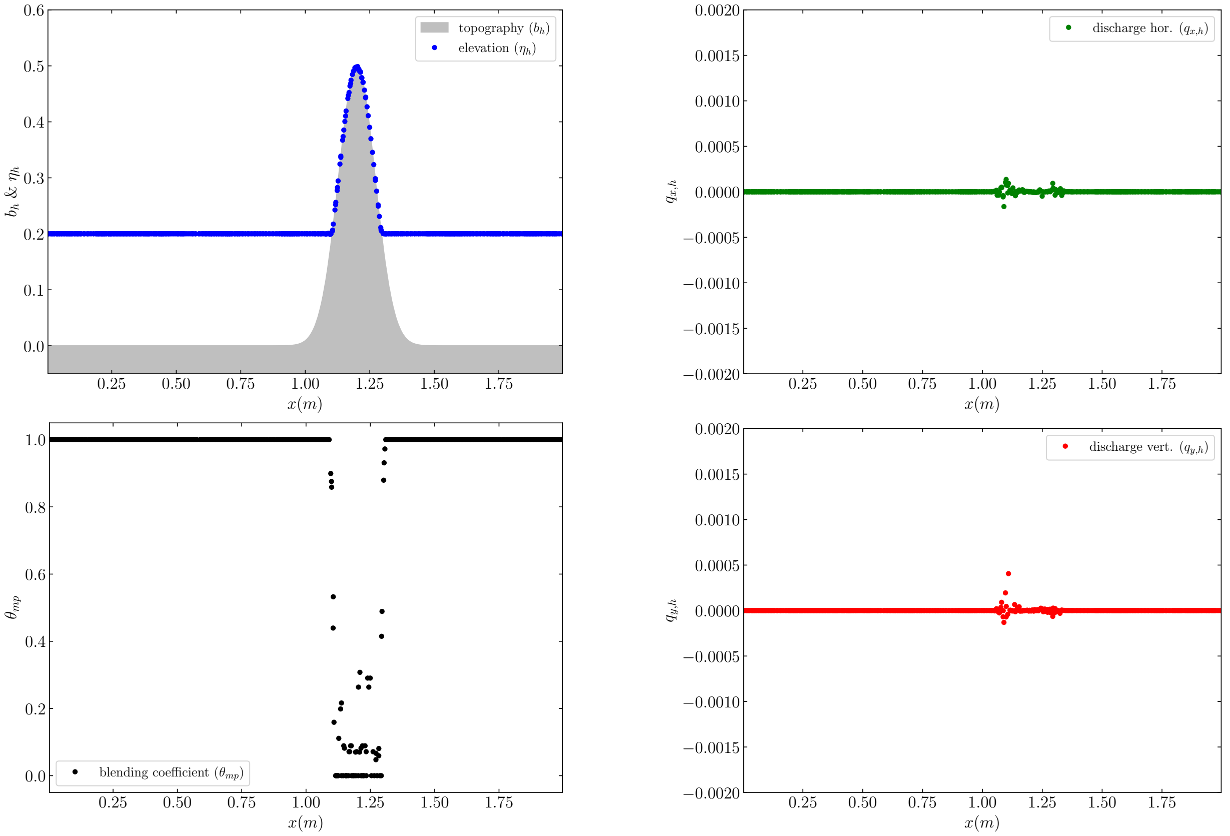

Figure 10: Well-balancing with dry area $-$ $\mathbb{P}^4$ solution on a domain slice ($y = 0.7$), located on the dry area.

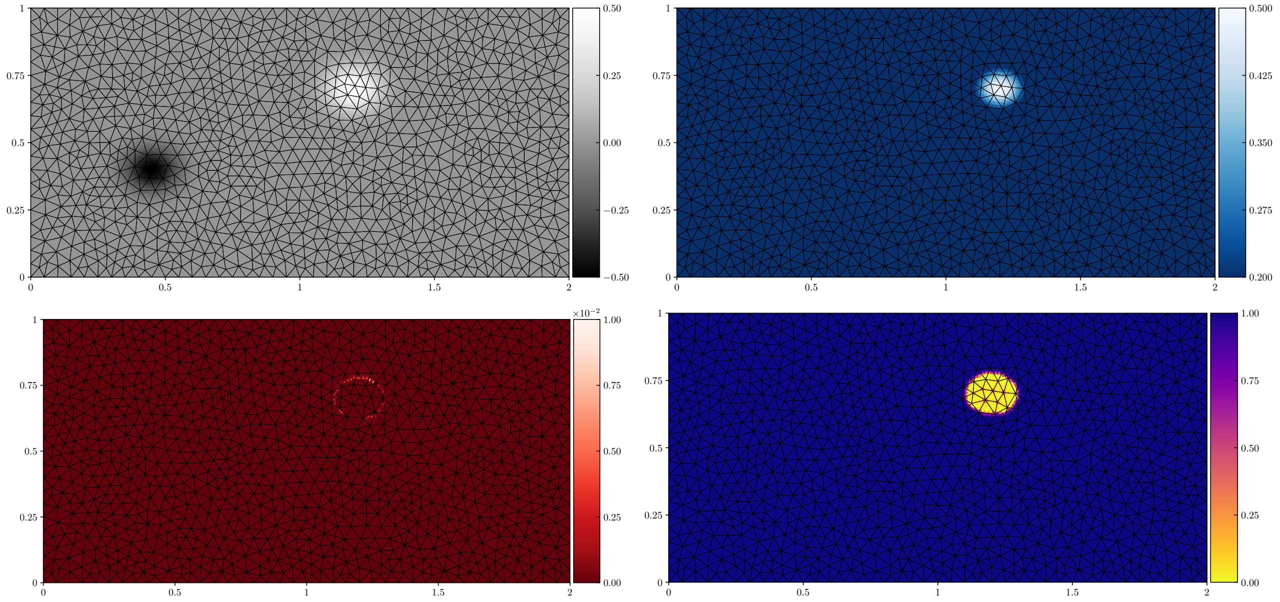

Figure 11: Well-balancing with dry area $-$ At $t = 20$ sec, from left to right and top to bottom: topography, free-surface elevation, discharge norm, and map of blending coefficient means per subcell.

direction), as show in Figures 12–13 and that even within such a demanding computational configuration, the numerical method still allows to sharply capture the propagating discontinuity and the rarefaction wave. This may be clearly observed in Figure 12 with a comparison between exact and numerical solutions on the whole domain, together with the related map of blending coefficients on the subcells, highlighting the efficiency of this *a priori* local corrections, only activated very locally in the vicinity of the solution's singularities, which is an optimal behavior generally observed only with *a posteriori* correction, showing again the practical efficiency of the relaxed subNAD.

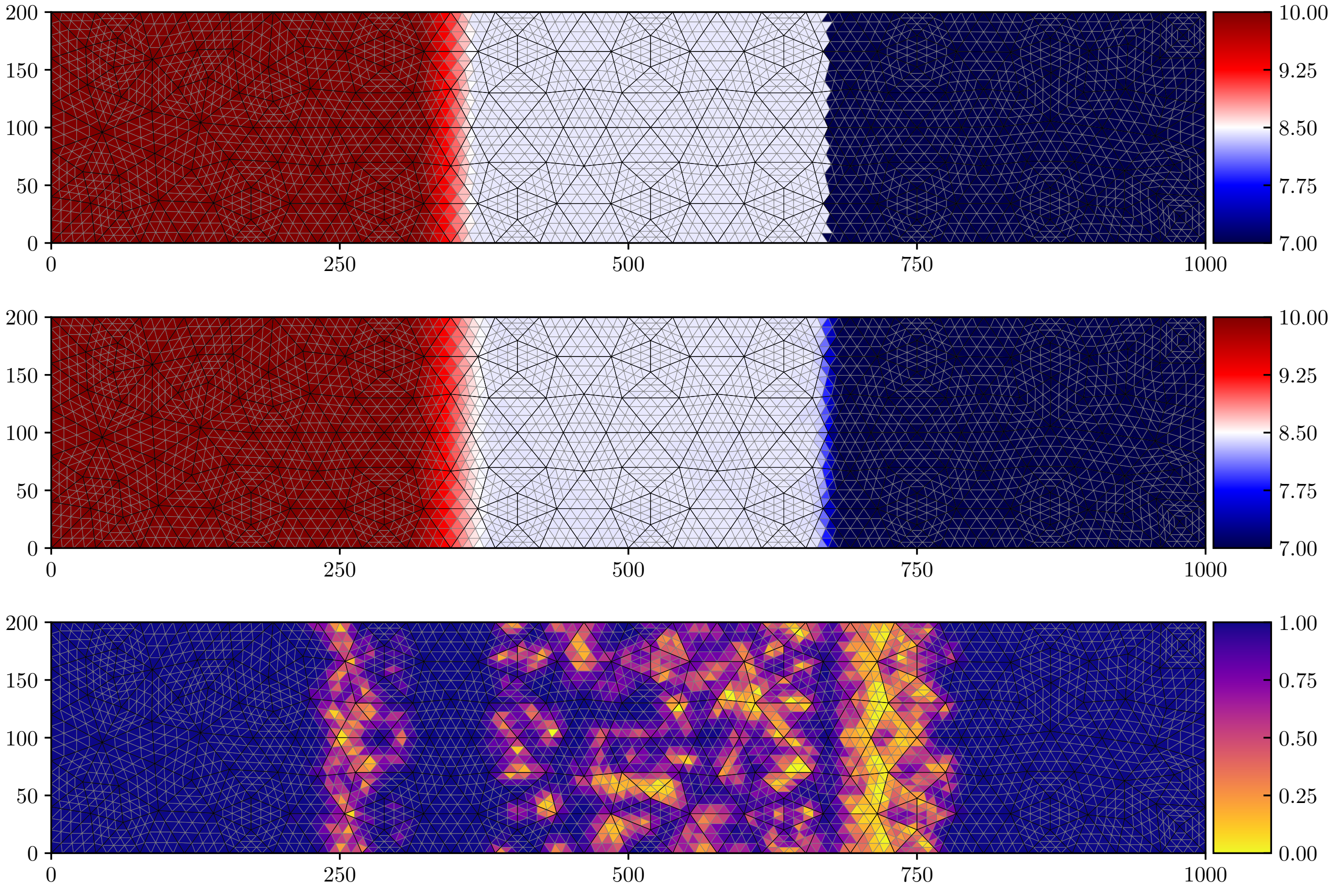

Figure 12: Dam-break on a wet-bed – At $t = 18$ sec, from top to bottom: exact elevation, numerical elevation, and map of blending coefficient means per subcell.

Indeed, the resulting numerical solution is in excellent agreement with the analytical solution, as observed on Fig.13 where a sliced solution is plotted, with the corresponding subcells values and compared with the exact solution. We also briefly show on Fig. 14 that (non-stiff) friction source terms may also be straightforwardly handled in the same way than the bathymetry source term, by further considering an additional Manning friction term, with $\gamma = \frac{10}{7}$ and several values of the Manning coefficient n_f, on the same mesh. Observing a consistent behavior, we choose not to further (quantitatively) investigate approximations of friction source terms and leave it for future works as extensions of [9, 25] for asymptotic parabolic regimes.

On a dry-bed

Simulation parameters.

Computational domain: $\Omega = [0, 1000] \times [0, 200]$
Number of cells: $n_{\text{el}} = 350$ cells (unstruct.), 240 cells (struct.)
Boundary conditions: solid walls

Polynomial degree: $k = 3$
Time-marching order: $p = 3$
Final time: $t_{\max} = 20, 60$ sec

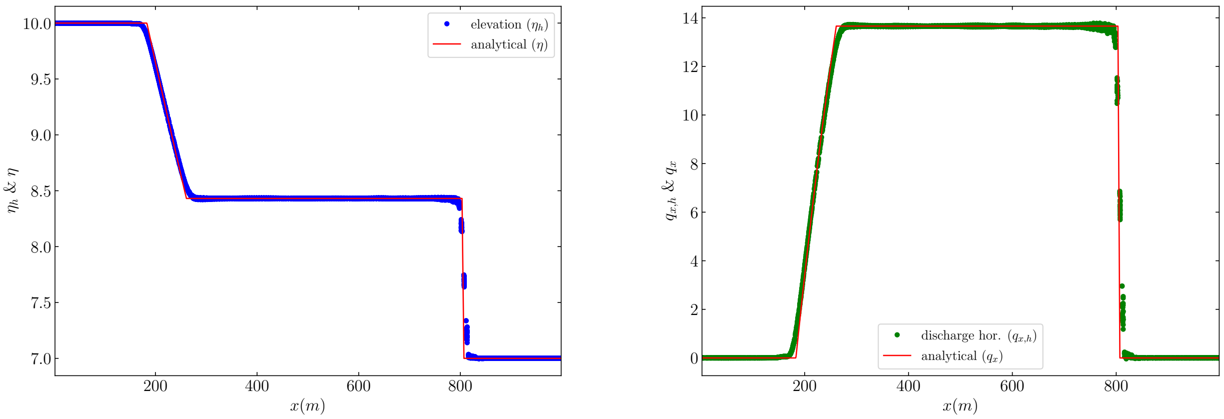

Figure 13: Dam-break on a wet-bed – $\mathbb{P}^4$ free-surface elevation and horizontal discharge density profiles at $t = 32$ sec.

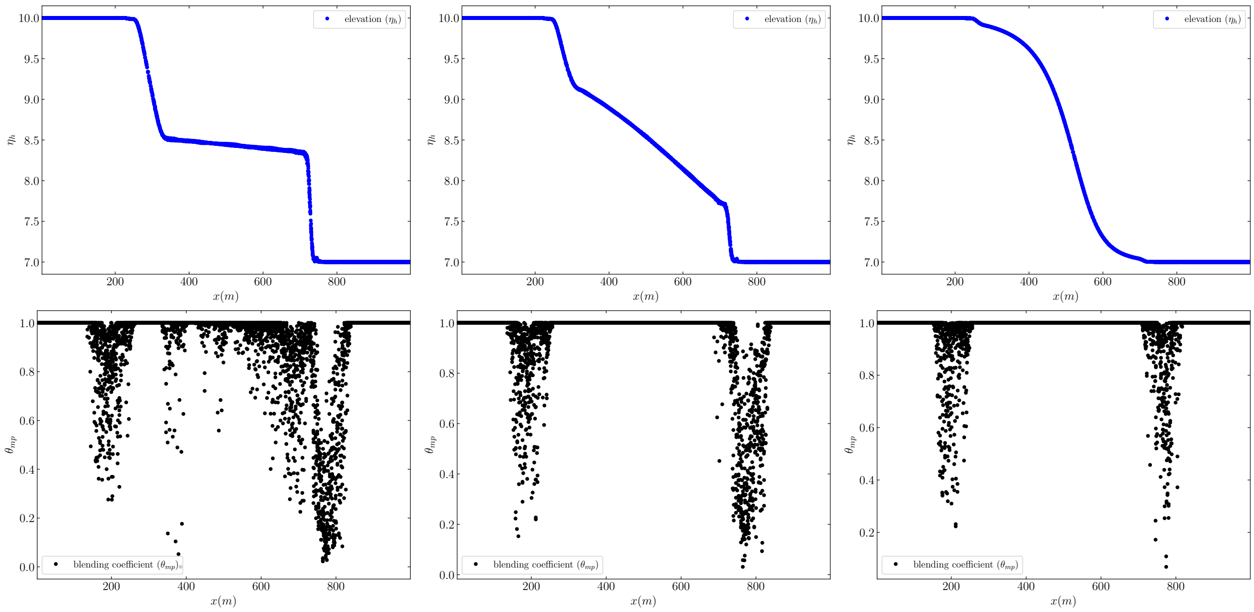

Figure 14: Dam-break on a wet-bed with nonlinear friction – $\mathbb{P}^4$ free-surface elevation and blending density profiles at $t = 24$ sec for $n_f = 0.5$ (left), 2 (center) and 10 (right).

Now, we set the initial-data as follows:

$$\eta(\boldsymbol{x},0) = \begin{cases} 10 & \text{if } x < 500, \\ 0 & \text{otherwise}, \end{cases} \qquad \mathbf{q}(\boldsymbol{x},0) = \mathbf{0},$$

resulting in a dam-break on a dry-bed, challenging the robustness of our method, and we show that the local subcell monolithic DG/FV scheme is able to accurately capture the flow's dynamic, while maintaining accuracy and robustness.

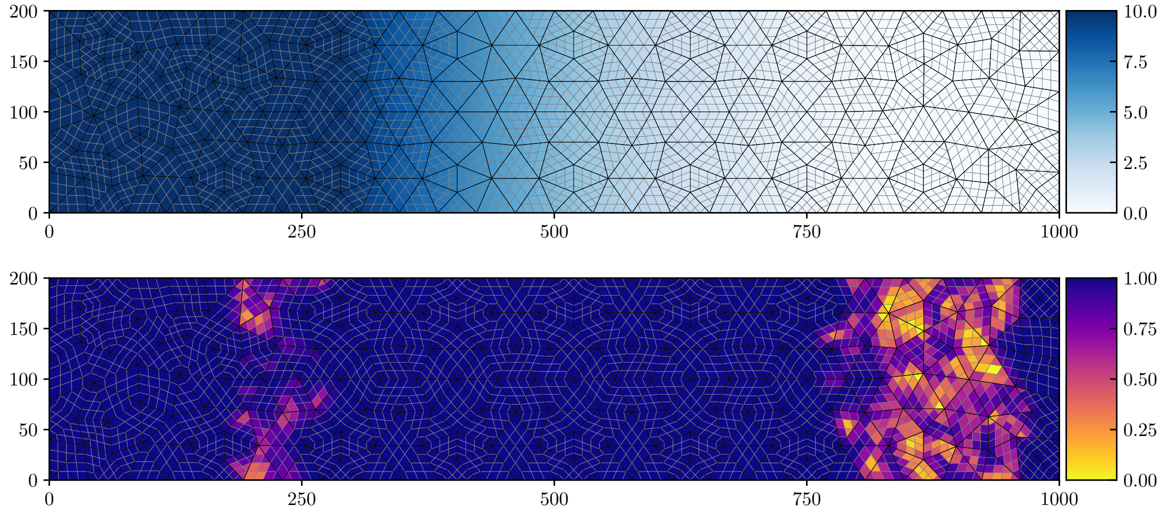

Figure 15: Dam-break on a dry-bed $-$ $\mathbb{P}^3$ free-surface and blending map with an unstructured mesh at $t = 20$ sec.

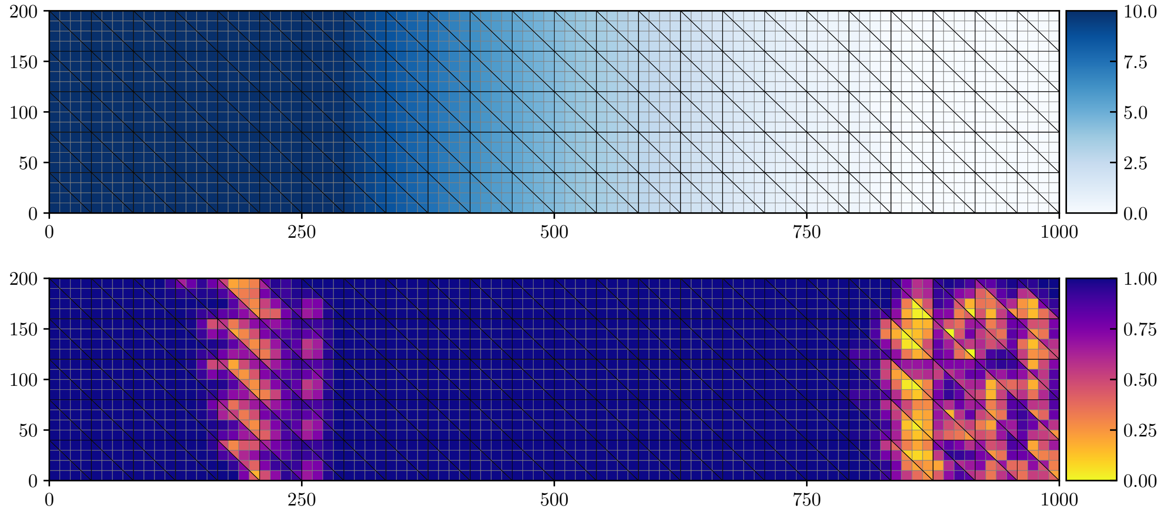

Figure 16: Dam-break on a dry-bed $-$ At $t = 20$ sec, $\mathbb{P}^3$ free-surface elevation and blending map on structured mesh.

Again, we consider our coarse unstructured mesh of 350 cells, together with an approximate piecewise-polynomial solution of degree $k = 3$. We emphasize that considering such a large mesh-size, the solution's singularities (wet-dry transitions) are again generally located inside mesh elements, exhibiting sub-mesh resolution capabilities and real efficiency and true robustness for higher-order approximations. We show in Figures 15 the approximate solution obtained at $t = 20$ sec. on the whole domain, together with the related map of blending coefficients on the subcells, assessing the practical efficiency of the PAD. Note that a comparison with the analytical solution is also shown for a sliced solution in the propagation direction in Figure 17, showing an excellent agreement,

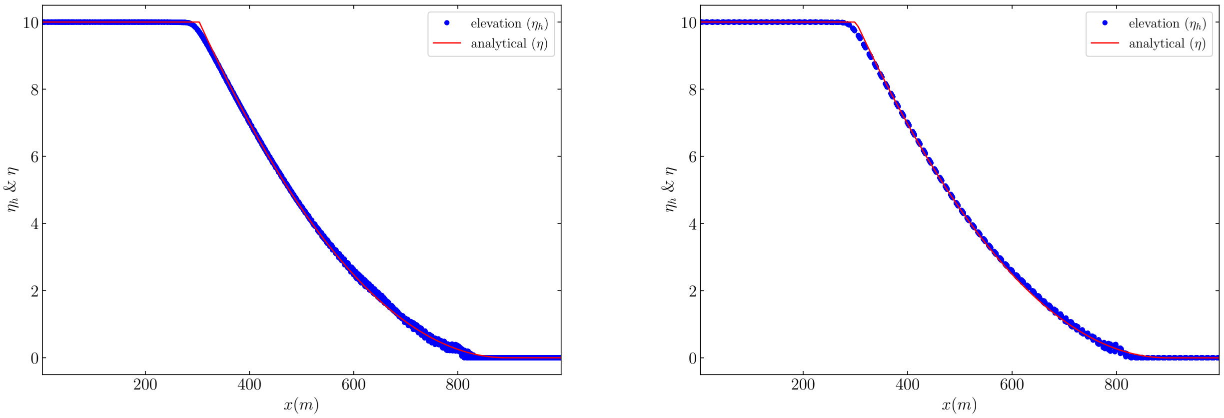

Figure 17: Dam-break on a dry-bed − Free-surface elevation profile for $\mathbb{P}^3$ solution on unstructured (left) and structured (right) meshes.

emphasizing again the chosen large mesh-size. To investigate the effect of mesh topology, we compare the approximate results obtained on both structured (240 elements) and unstructured meshes, as shown in Figure 16. We observe only marginal differences, which confirms that the chosen corrective mechanisms are activated in similar areas. This demonstrates the robustness and flexibility of the scheme with respect to the mesh choice. A comparison between the analytical solution and numerical results for both mesh types at $t = 20\,s$ is also presented in Figure 17.

5.4. Circular dam-break

Simulation parameters.

Computational domain: $\Omega = \{\boldsymbol{x} \in \mathbb{R}^2 \mid x^2 + y^2 \leq 10^2\}$
Number of cells: $n_{\text{el}} = 870$ cells
Boundary conditions: homogeneous Neumann

Polynomial degree: $k = 4$
Time-marching order: $p = 3$
Final time: $t_{\max} = 1$ sec

In this fourth test-case, we study the dam-break with a radial symmetry, in a circular computational domain, in order to produce a solution with true two-dimensional features and symmetry (again, the topography is set to $b(\boldsymbol{x}) = 0$). Such a circular dam-break problem on a dry bed is a classic yet highly challenging benchmark for evaluating the robustness and accuracy of numerical schemes. Its complexity stems from several critical factors which are combined: i) the transition to a dry bed combined to the radial symmetry preservation (maintaining the circularity of the solution on non-radial grids to assess the scheme's anisotropy), ii) wave focusing and singularities: as the depression wave propagates toward the center, the convergence of flow leads to a geometric focalization. This concentration of energy tests the scheme's ability to handle high gradients and sharp transitions without generating spurious oscillations associated to Gibbs phenomenon, iii) shock-capturing for high-order methods, as the initial discontinuity represents a severe test for high-order methods. In the following, we show that the proposed scheme clearly resolves the resulting complex and combined 2D wave patterns.

On a wet-bed

The initial-data is set as follows:

$$\eta(\boldsymbol{x}, 0) = \begin{cases} 1.5 & \text{if } \sqrt{x^2 + y^2} < 4, \\ 0.5 & \text{otherwise.} \end{cases}, \qquad \mathbf{q}(\boldsymbol{x}, 0) = \mathbf{0}.$$

Free-surface elevation and discharge norm respectively computed at some intermediate (left) and final (right) times are shown in Figure 18, while some one-dimensional sliced profiles obtained along the horizontal and vertical axes are reported in Figure 19. Compared against a first-order FV baseline on a very fine grid, our numerical solution preserves excellent radial symmetry throughout the simulation, even on such a coarse unstructured mesh. The circular front remains perfectly isotropic, with no visible grid-deformation effects or 'squaring' of the wave as observed with cartesian meshes. Also, the wave focusing at the center is handled without any spurious oscillations: the peak water height at the moment of convergence is in close agreement with reference solutions, demonstrating the effectiveness of the proposed method and again, the sub-grid resolution capabilities.

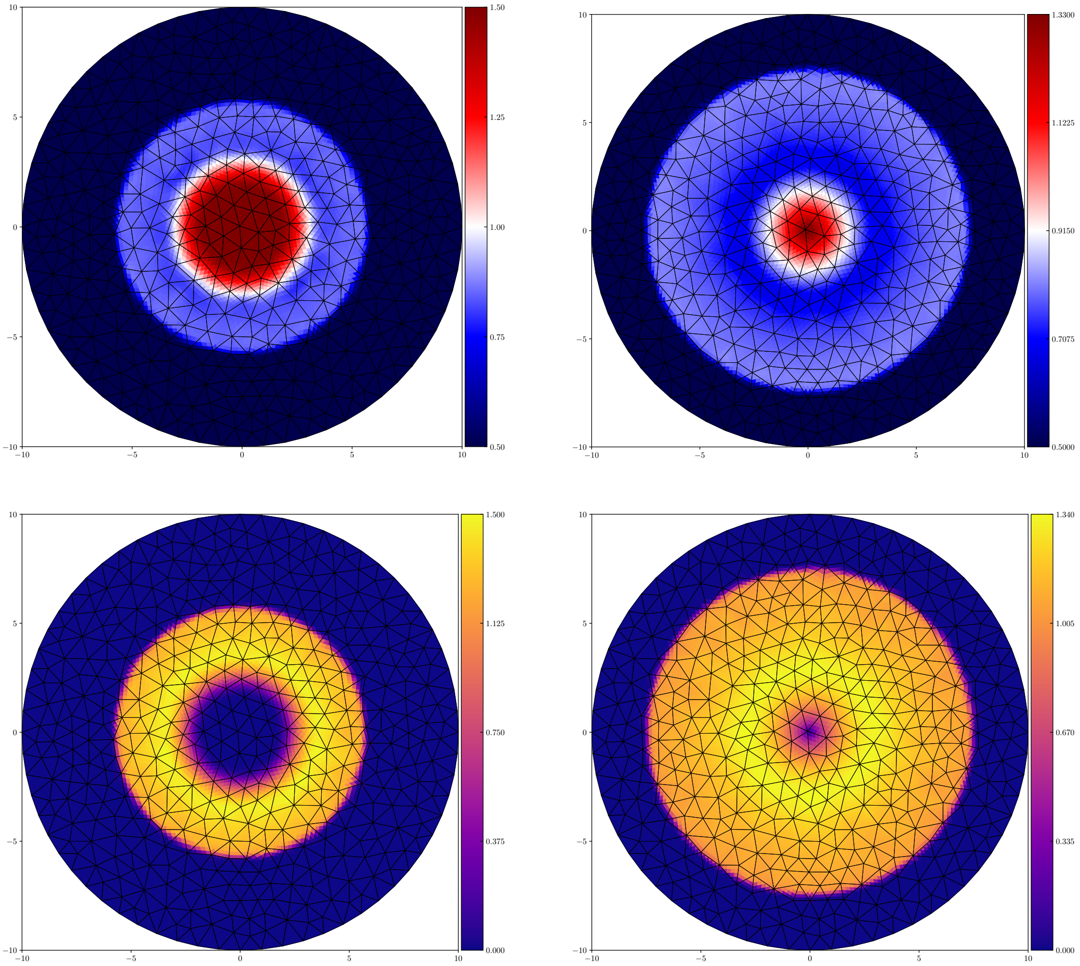

Figure 18: Circular dam-break on a wet-bed – $\mathbb{P}^4$ free-surface elevation (top) and discharge norm (bottom) at $t = \frac{t_{\max}}{2}$ (left) and at $t = t_{\max}$ (right).

On a dry-bed

Now, let consider the case of an initially dry area:

$$\eta(\boldsymbol{x}, 0) = \begin{cases} 1.5 & \text{if } \sqrt{x^2 + y^2} < 4, \\ 0 & \text{otherwise}, \end{cases}, \qquad \mathbf{q}(\boldsymbol{x}, 0) = \mathbf{0}.$$

We show on Figure 20 the free-surface elevation at final time on the computational domain (left), together with the corresponding colormap of the blending coefficients, automatically adapted to ensure stability. Again, we observe some very satisfying results, as confirmed on Figure 21 where the free-surface elevation (left) and related blending coefficients (right) at $t = t_{\max}$ on slice $y = 0$ are displayed. The scheme demonstrates strict positivity-preserving properties at the wet/dry interface. No non-physical negative water-depths were observed, and the wetting-drying front is captured sharply without the need for excessive *a priori* corrections.

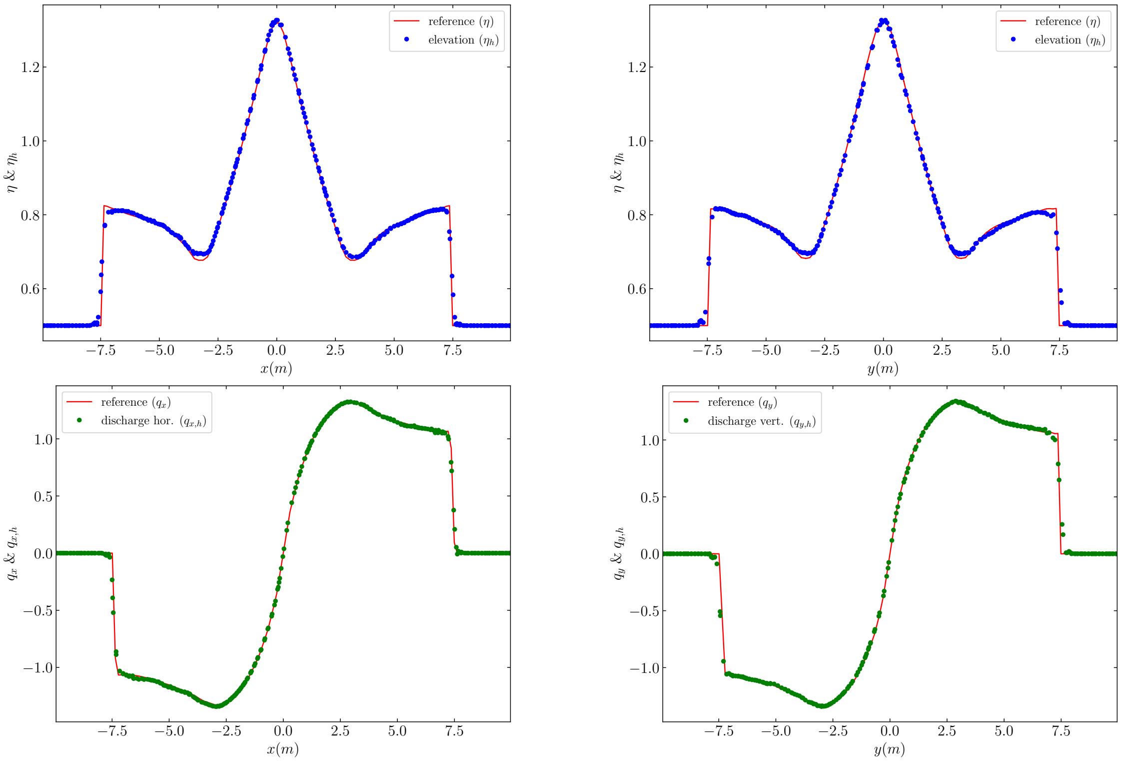

Figure 19: Circular dam-break on a wet-bed $-$ $\mathbb{P}^4$ free-surface elevation at $t = t_{\max}$ on slice $y = 0$ (resp. $x = 0$) and horizontal (resp. vertical) discharge.

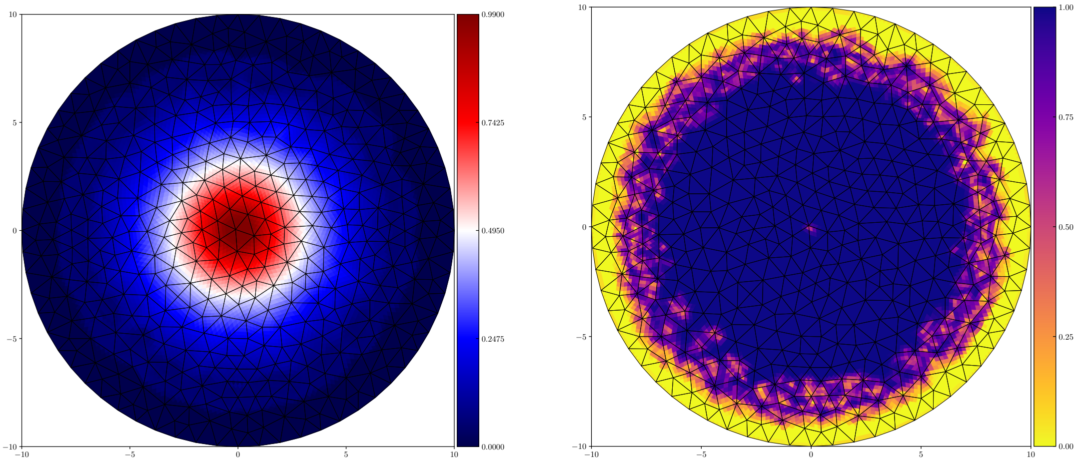

Figure 20: Circular dam-break on a dry-bed $-$ $\mathbb{P}^4$ free-surface elevation (left) and blending coefficients (right) at $t = t_{\max}$.

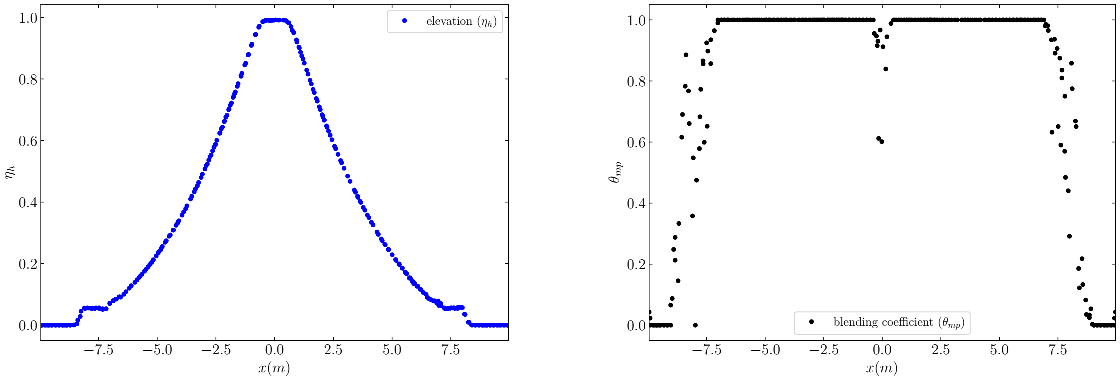

Figure 21: Circular dam-break on a dry-bed – $\mathbb{P}^4$ free-surface elevation (left) and blending coefficients (right) at $t = t_{\max}$ on slice $y = 0$.

5.5. Carrier-Greenspan solutions

Transient solution

Simulation parameters.

Computational domain: $\Omega = [-20, 6] \times [0, 4]$
Number of cells: $n_{\text{el}} = 1092$ cells
Boundary conditions: prescribed Dirichlet (left), homogeneous Neumann (right)

Polynomial degree: $k = 2$
Time-marching order: $p = 1$
Final time: $t_{\max} = 100$ sec

In order to combine moving wet-dry contact lines with varying bathymetry, we consider the test-case originally introduced by Carrier in [13], modeling evolutions of the surface-elevation near the shoreline of a sloping beach, from an initially depressed and held stationary configuration, before being released at $t = 0$. This setup generates a transient wave that moves up the beach and eventually returns to equilibrium through a slow convergence process. It offers an excellent benchmark to assess the robustness of the monolithic DG/FV scheme when dealing with long-wave run-up problems.

In [13], an analytical solution to the NSW equations is obtained using a hodograph transformation, introducing two dimensionless variables, σ^* and λ^*, which act respectively as space-like and time-like coordinates:

$$\sigma^* = 4c^*, \quad \lambda^* = 2\left(u^* + t^*\right).$$

Let l denote the characteristic length and α the beach slope. The dimensionless variables are defined using the following scaling:

$$x^* = x/l, \quad \eta^* = \eta/(\alpha l), \quad u^* = u/\sqrt{\mathrm{g}\alpha l}, \quad t^* = t/\sqrt{l/(\alpha g)}, \tag{28}$$

and the non-dimensional phase speed is given by

$$c^* = \sqrt{\eta^* - x^*}. \tag{29}$$

The initial-data for the solution is specified as:

$$\eta_0^*(\sigma^*) = e\left(1 - \frac{5}{2}\frac{a^3}{(a^2+\sigma^{*2})^{\frac{3}{2}}} + \frac{3}{2}\frac{a^5}{(a^2+\sigma^{*2})^{\frac{5}{2}}}\right), \qquad \mathbf{q}_0^*(\sigma^*, \cdot) = \mathbf{0}, \qquad x^* = -\frac{\sigma^{*2}}{16} + \eta_0^*,$$

where $a = \frac{3}{2}(1 + 0.9e)^{1/2}$, and e is a small parameter characterizing the initial surface depression.

In the following, we choose $e = 0.1$, $\alpha = 1/50$, the initial free-surface profile is expressed in dimensional form, with $l = 20$ m and the analytical variation of the free-surface elevation at the offshore boundary is prescribed as the inlet boundary condition to drive the motion. The evolution of the free-surface during the transient phase is displayed in Figure 22. At $t = 10$ sec, a direct comparison between the analytical and numerical elevations is shown in Figure 23, while the horizontal discharge profiles and the final elevation profile are illustrated in Figure 24. The numerical results for the Carrier-Greenspan test case demonstrate the significant advantages of the high-order local subcell monolithic DG/FV scheme. Even when operating on such a coarse unstructured mesh, the scheme accurately captures the non-linear oscillation and the precise movement of the shoreline. The high-order sub-grid representation within each element compensates for the limited spatial resolution of the global mesh, preserving the analytical wave profile with minimal dissipation. This performance highlights the ability of the method to resolve complex run-up and draw-down dynamics on irregular geometries without the numerical damping typically associated with low-order approximations on similar under-resolved grids.

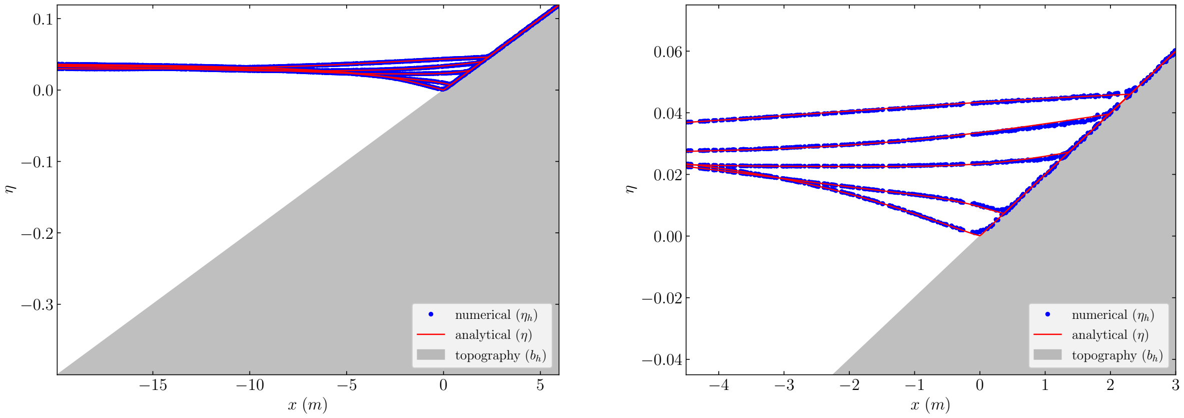

Figure 22: Carrier & Greenspan transient solution − Snapshots of $\mathbb{P}^2$ free-surface elevation profile on full domain (left) and zoom on dry-bed (right) for $t \in [1, 21]$ sec.

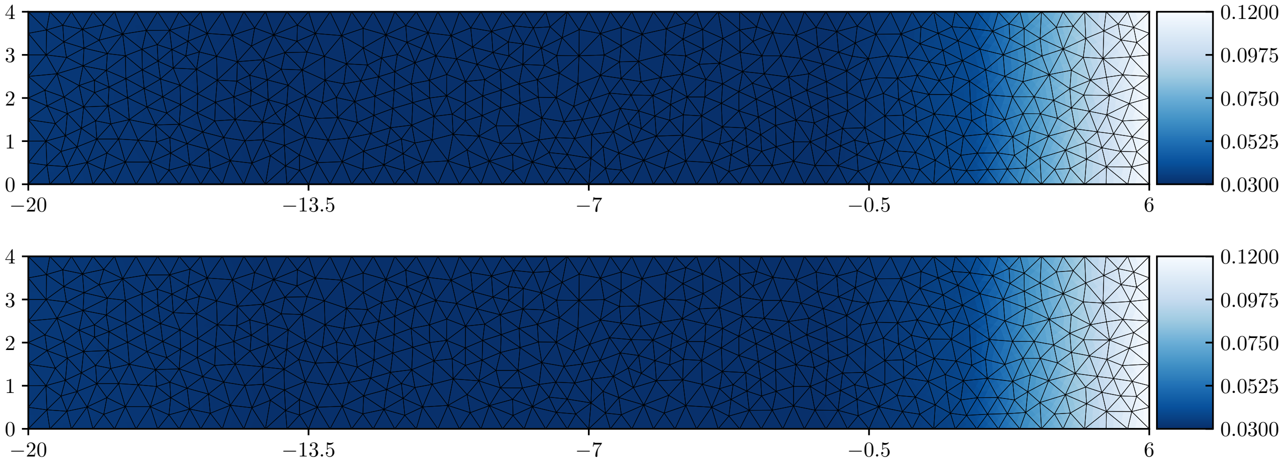

Figure 23: Carrier & Greenspan transient solution − At $t = 10$ sec, exact elevation (top) and $\mathbb{P}^2$ numerical elevation (bottom).

Periodic solution

Simulation parameters.

Computational domain: $\Omega = [-20, 6] \times [0, 4]$
Number of cells: $n_{\text{el}} = 1092$ cells
Boundary conditions: prescribed Dirichlet (left), homogeneous Neumann (right)

Polynomial degree: $k = 2$
Time-marching order: $p = 1$
Final time: $t_{\max} = 300$ sec

This benchmark models the run-up and run-down of a monochromatic wave propagating over a plane beach. The dimensionless amplitude of the periodic wave is denoted by A^* and its frequency by ω^*. As the wave moves toward the shore and reflects back into the sea, it generates a standing wave-pattern over the sloping bottom.

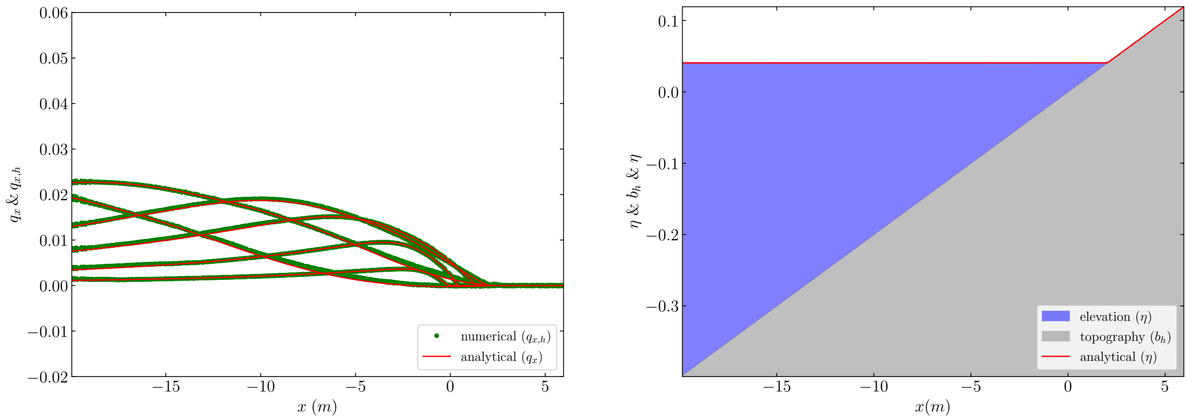

Figure 24: Carrier & Greenspan transient solution – Snapshots of $\mathbb{P}^2$ horizontal discharge density profile for $t \in [1, 21]$ sec (left) and elevation profile at final time (right).

Using the dimensionless variables introduced in (28) and (29), the analytical solution is given by:

$$\begin{cases} u^* = -\dfrac{A^* J_1(\sigma^*) \sin(\lambda^*)}{\sigma^*}, \\ \eta^* = \dfrac{A^*}{4} J_0(\sigma^*) \cos(\lambda^*) - \dfrac{u^{*2}}{4}, \\ t^* = \dfrac{1}{2}\lambda^* - u^* \quad \text{and} \quad x^* = \eta^* - \dfrac{\sigma^{*2}}{16}, \end{cases}$$

where J_0 and J_1 denote the Bessel functions of the first kind of order zero and one, respectively. We set $A^* = 0.6$ and $\omega^* = 1$, corresponding to a non-breaking wave, with a reference length $l = 20$ m and a beach slope of $\alpha = 1/30$. The solution at $t = 0$ is used as the initial-data, and, similarly to the previous transient case, the analytic solution at the offshore boundary is prescribed as the inlet boundary condition, driving the motion. For a detailed description, we refer again to [13]. The simulation is carried out up to $t_{\max} = 1.5\,T$, where T is the period of the external forcing. The spatio-temporal evolution of the free-surface is illustrated in Figure 25. The quality of the results is once again clear, showing an excellent agreement with the expected wave run-up and run-down patterns. The local subcell monolithic DG/FV scheme approximation effectively resolves the non-linear transformation of the wave profile as it approaches the shore, maintaining a sharp and oscillation-free representation of the moving boundary. Even throughout multiple oscillation cycles, the numerical solution shows no sign of amplitude decay or phase shift, confirming the low-dissipative nature of the high-order scheme. This highlights the robustness of the wet/dry front treatment in capturing the periodic shoreline migration over the sloping beach. Notably, these results are achieved using a very coarse and non-matching mesh, reflecting the demanding conditions typically encountered in operational engineering contexts. The ability of the scheme to maintain high fidelity under such under-resolved constraints further underscores its

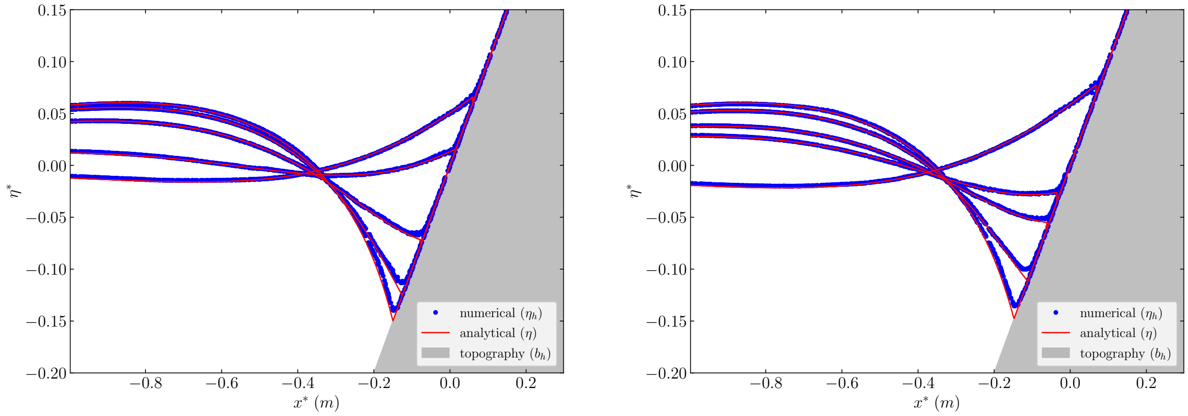

Figure 25: Carrier & Greenspan periodic solution – Snapshots of $\mathbb{P}^2$ free-surface elevation profile for $t \in [80, 86]$ sec (left) and for $t \in [154, 160]$ sec (right).

suitability for practical large-scale applications. As a first step towards such applications, we investigate some more demanding test-cases in the remainder of this section.

5.6. Wave-island interactions

Single-wave on a conical island

Simulation parameters.

Computational domain: $\Omega = [0, 25] \times [0, 30]$
Number of cells: $n_{\text{el}} = 13500, 6000, 3150$ cells
Boundary conditions: solid walls (top and bottom), inflow (left) and Neumann (right)

Polynomial degree: $k = 1, 2, 3$
Time-marching order: $p = 3$
Final time: $t_{\max} = 10$ sec

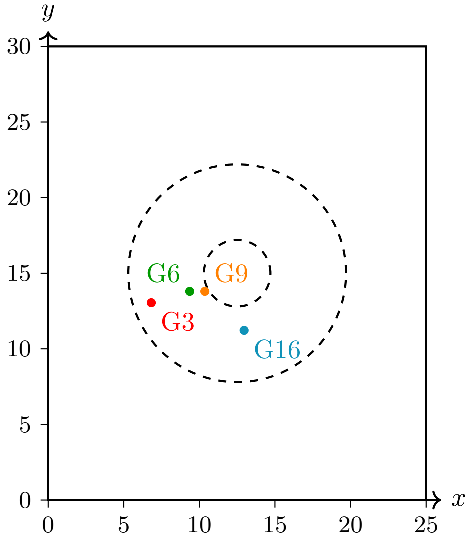

Figure 26: Single-wave on a conical island - Experimental setup : computational domain with island geometry and gauge locations.

In this subsection, we investigate a test case directly inspired by the experimental setup of Liu et al. [49]. It consists of a solitary wave propagating and running up over an idealized conical island within a rectangular basin. The wave possesses sufficient initial amplitude and energy to produce significant run-up on both the front and lee sides of the island. Consequently, this test case evaluates the robustness of the numerical method under challenging and physically realistic conditions.

Experimental data are available from a series of gauges distributed around the island. In the laboratory experiments, the solitary wave shoals and breaks on the front slope, with the peak impact recorded at gauge 9 ($t \approx 5.6$ s). The wave energy is subsequently partitioned and refracted around the island, leading to a secondary run-up on the rear side at gauge 16 ($t \approx 9.7$ s), while a circular reflected front propagates away from the obstacle. Subsequent wave splitting and backwash processes generate secondary oscillations, particularly in the sheltered region behind the island. These phenomena have been numerically reproduced in numerous studies and serve as a standard benchmark for model validation.

Following the original experimental description, the island bathymetry $b(r)$ is modeled as:

$$b(r) = \begin{cases} \max\left(0.625,\, 0.9 - \frac{r}{4}\right), & r < 3.6, \\ 0, & \text{otherwise}, \end{cases} \tag{30}$$

where r denotes the radial distance from the center of the island. The quiescent water depth is set to $h_0 = 0.32$. The incident wave is generated via a time-dependent boundary condition:

$$\begin{cases} h(t) = h_0 + \alpha h_0 \operatorname{sech}^2\left(\dfrac{\sqrt{g h_0}}{L}\chi t\right), \\ \chi = \sqrt{\dfrac{3\alpha}{4\beta}(1+\alpha)}, \quad \beta = \left(\dfrac{h_0}{L}\right)^2, \quad L = 15, \quad \alpha = 0.3, \end{cases} \tag{31}$$

although there is no consensus concerning this standard solitary wave forcing. A schematic of the computational setup and gauge locations is provided in Figure 26, while the comparison between numerical results and experimental data is presented in Figure 27. In the present study, we perform simulations using polynomial orders

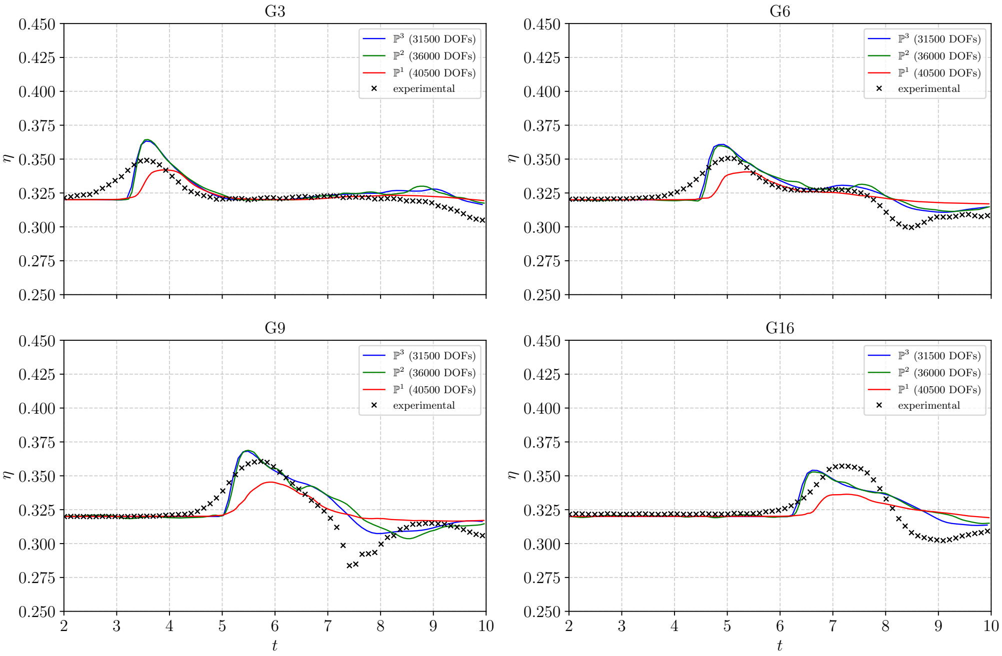

Figure 27: Single-wave on a conical island - Numerical/experimental comparisons of the time-series of the surface-elevation at the different gauges for $t \in [2, 10]$ sec.

$\mathbb{P}^1$ (13,500 cells), $\mathbb{P}^2$ (6,000 cells), and $\mathbb{P}^3$ (3,150 cells). The resulting free-surface elevations are compared with experimental time-series at selected gauges, as shown in Figure 27. The good agreement between numerical results and experimental data confirms the ability of the solver to capture the primary features of the wave–island interaction. This includes the breaking-induced run-up on the front slope and the delayed response at the rear gauges, demonstrating that the contact-line velocity around the island is accurately estimated. While higher-order schemes notably improve both phase and amplitude accuracy, some discrepancies persist in the backwash oscillations. These differences are classically attributed to dispersive effects, which are not accounted for in the hyperbolic Nonlinear shallow-water (NSW) equations.

We emphasize that to maintain a consistent computational resolution, the mesh resolution is adjusted such that the total number of degrees of freedom remains within the same order of magnitude as the polynomial degree increases. Despite a slight reduction in the actual number of DOFs for higher orders, the $\mathbb{P}^3$ scheme yields the most accurate results. We observe a particularly significant improvement when moving from $\mathbb{P}^1$ to $\mathbb{P}^2$, while the gain between $\mathbb{P}^2$ and $\mathbb{P}^3$ is more incremental, but entails a substantial reduction in the number of mesh elements.

It is worth noting that these results are obtained on meshes significantly coarser than those typically reported in the literature, where simulations often involve one to two orders of magnitude more elements. Even without local mesh refinement around the island or in the vicinity of the gauges, the present method successfully reproduces the primary wave characteristics observed in the experiments. This highlights the ability of high-order schemes to provide accurate and robust solutions on relatively modest computational grids, while suggesting that further improvements could be achieved with local refinement.

In particular, an artificial viscosity coefficient could be introduced, as is common practice in industrial codes. Furthermore, adopting a dispersive model would likely better capture the complex wave interactions, especially in the sheltered region behind the island. However, the objective here was primarily to evaluate the scheme in a standard, “ready-to-use” form. Finally, it should be noted that, to the authors’ knowledge, a definitive consensus on the optimal setup for this benchmark has yet to be established—and this study does not claim to provide one.

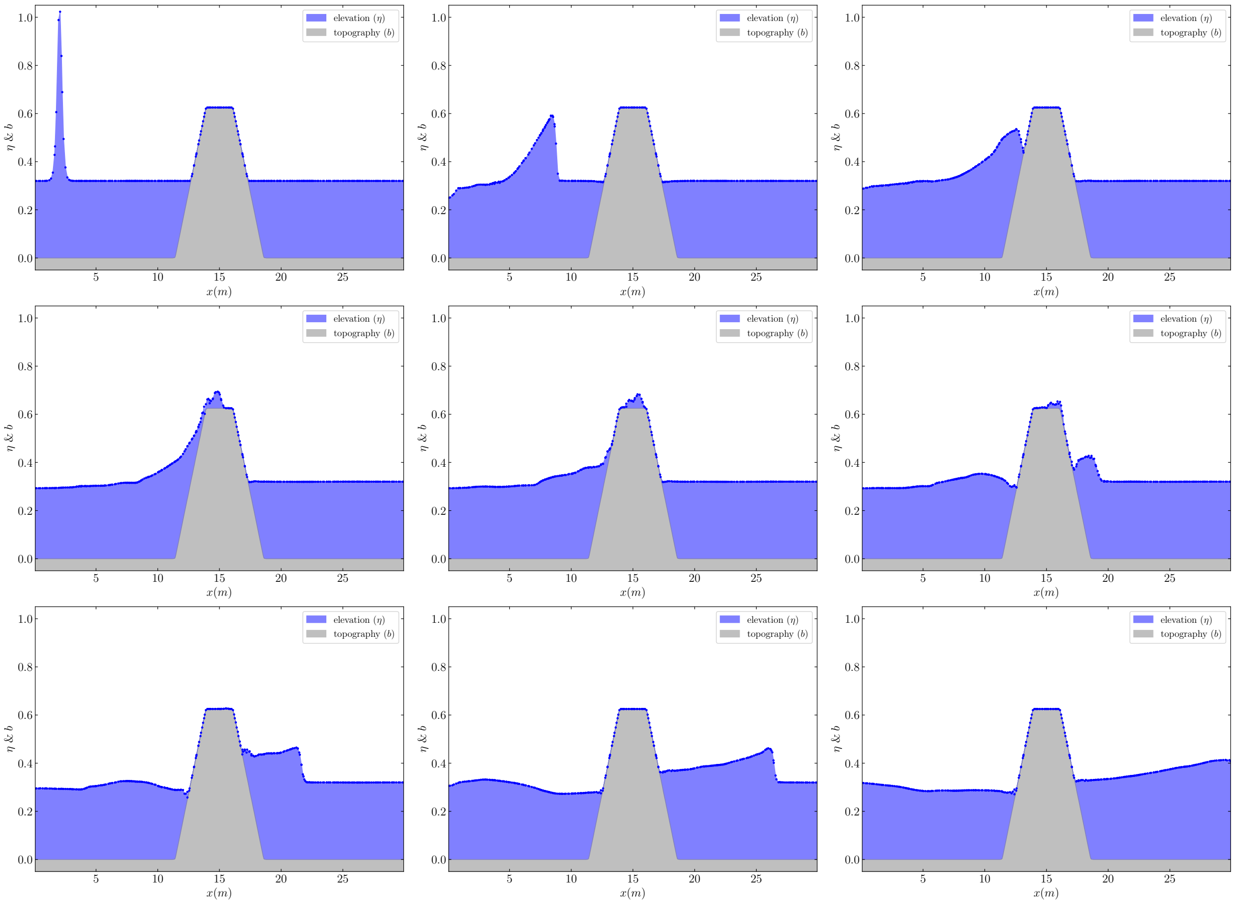

Figure 28: Tidal-wave overtopping the conical island – Snapshots of $\mathbb{P}^2$ free-surface elevation on slice $y = 12.5$ for $t \in [0, 12]$ sec.

Tidal-wave overtopping the conical island

Simulation parameters.

Computational domain: $\Omega = [0,30] \times [0,25]$
Number of cells: $n_{\text{el}} = 3790$ cells
Boundary conditions: solid walls (top and bottom), Dirichlet (left and right)

Polynomial degree: $k = 2$
Time-marching order: $p = 3$
Final time: $t_{\max} = 12$ sec

To conclude this subsection on wave–structure interactions, we quantitatively investigate the effect of a higher wave amplitude by reproducing the configuration recently proposed in [35]. Unlike the previous benchmark, this case features a traveling wave with sufficient initial amplitude and energy to fully overtop the island, thereby demonstrating the robustness of the method under even more dynamic and challenging conditions. We briefly recall the specific parameters for this setup, which involves slight modifications from the previous case, with the bottom topography defined as:

$$b(\boldsymbol{x}) := \min\left(H_{\text{top}}, \left(H_{\text{cone}} - \frac{r(\boldsymbol{x})}{s_{\text{cone}}}\right)_+\right), \quad \text{where} \quad r(\boldsymbol{x}) := \sqrt{(x-15)^2 + (y-12.5)^2}.$$

Here, $H_{\text{top}} = 0.625$, $H_{\text{cone}} = 0.9$, and $s_{\text{cone}} = 4$ (all dimensions in meters). The initial-data is chosen to model a solitary wave approaching the island from the left. The initial water-height and horizontal velocity are defined as:

$$\begin{aligned} H(\boldsymbol{x},0) &:= \left(H_0 + \frac{A}{\cosh^2\left(\sqrt{\frac{3A}{4H_0^3}}(x-x_s)\right)} - b(\boldsymbol{x})\right)_+, \\ u(\boldsymbol{x},0) &:= \frac{A}{\cosh^2\left(\sqrt{\frac{3A}{4H_0^3}}(x-x_s)\right)}\sqrt{\frac{g}{H_0}}, \end{aligned}$$

with the parameters $h_0 = 0.32$, $A = 2.5h_0$, and $x_s = 2.04$. The initial momentum is subsequently defined as $\mathbf{q}(\boldsymbol{x},0) = (u(\boldsymbol{x},0)h(\boldsymbol{x},0),0)^\top$. The time evolution of the free-surface elevation along the horizontal cross-section at $y = 12.5$ is presented in Figure 28. A complementary view of the two-dimensional free-surface elevation and the corresponding blending maps at various stages of the simulation is provided in Figure 29. For this final test case, we emphasize that only 3,700 mesh elements are employed. This clearly demonstrates the ability of the proposed method to ensure both accuracy and robustness on very coarse meshes, highlighting its suitability for operational purposes, where bathymetry and computational grids are often constrained by low-resolution experimental measurements.

6. Conclusion

In this work, we have developed a high-order monolithic DG/FV framework for the two-dimensional nonlinear shallow-water equations on unstructured meshes. The core of the method lies in a subcell sub-partitioning that allows for a unified interpretation of the DG discretization. By employing convex blended fluxes, the scheme ensures key admissibility properties at the discrete level, with particular emphasis on positivity-preservation and well-balanced source term treatment for the preservation of motionless steady states.

The numerical results clearly demonstrate the effectiveness of this approach across a range of scenarios, including challenging test cases with wet/dry interfaces and complex bathymetries. The strategy successfully suppresses spurious oscillations while maintaining high-order accuracy in smooth regions, offering a compelling compromise between robustness and precision, even on relatively coarse grids, as expected for operational purpose.

Future research will focus on coupling this framework with two-dimensional floating-structure models. Additionally, we plan to extend the method to an Arbitrary Lagrangian-Eulerian (ALE) framework to handle moving meshes, a critical requirement for coastal engineering and complex wave–structure interactions. We anticipate that the present method will serve as a robust and accurate foundation for addressing these advanced computational challenges.

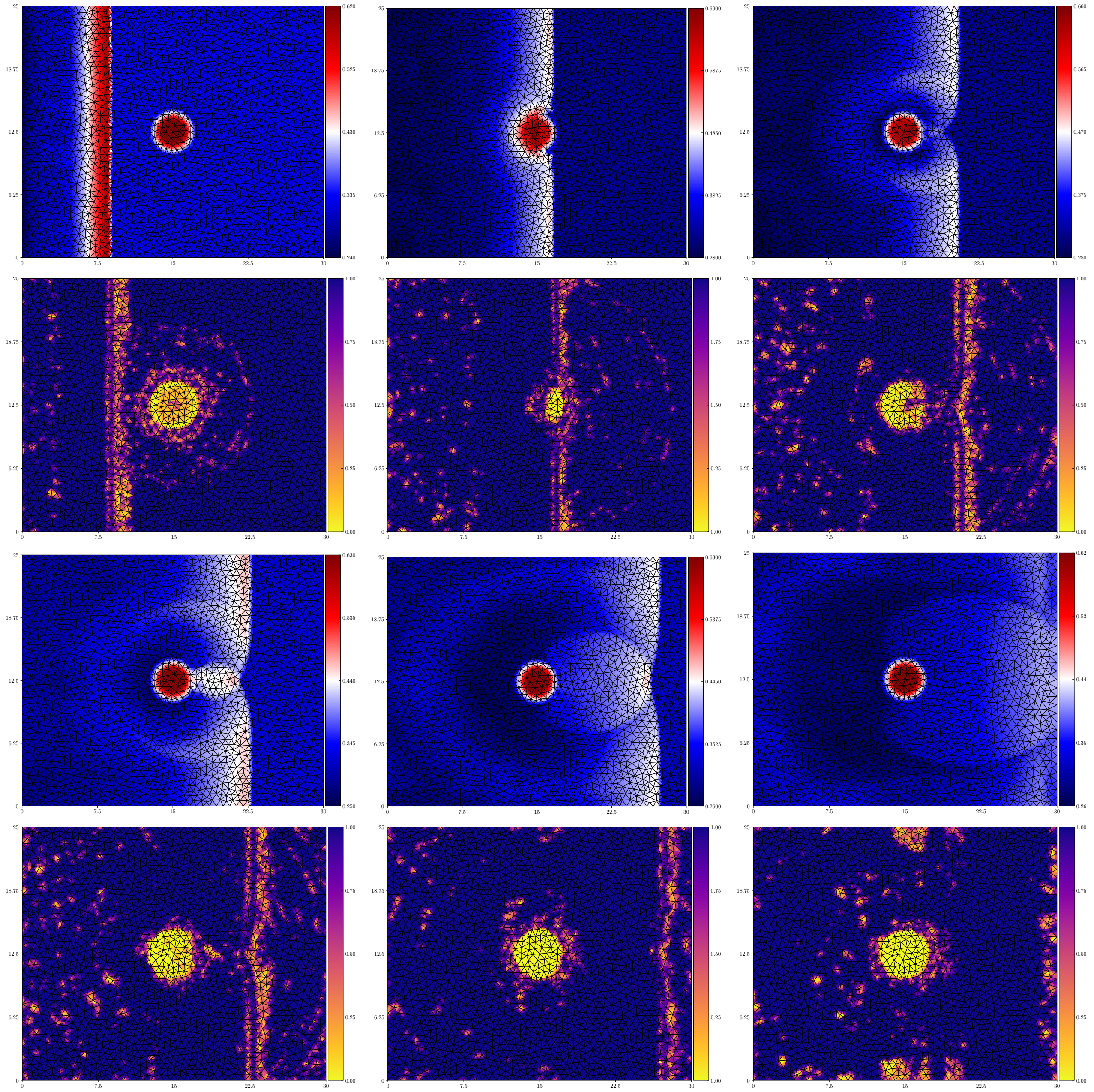

Figure 29: Tidal-wave overtopping the conical island – Snapshots of $\mathbb{P}^2$ free-surface elevation (1^{st} and 3^{rd} line) and their corresponding blending map (2^{nd} and 4^{th} line) for $t \in [1, 12]$ sec.

Appendix A: proof of Lemma

Proof. Noticing that numerical flux term

$$\sum_{S_p^v \in \mathscr{V}_m^c} \int_{\Gamma_{mp}^c} \widehat{\mathbb{F}}_n \,\mathrm{d}s = \sum_{S_p^v \in \mathscr{V}_m^c} \int_{\Gamma_{mp}^c} \mathbb{F}_h^c \cdot \mathbf{n}_{mp} \,\mathrm{d}s - \sum_{k=1}^{\#\mathscr{F}_c} \int_{\Gamma_{cv(k)}^c} \left(\mathbb{F}_h^c \cdot \mathbf{n}_{cv(k)} - \mathbb{F}^*_{cv(k)} \right) \widetilde{\psi}_m^c \,\mathrm{d}s,$$

can be equivalently written as

$$\int_{\partial S_m^c} \widehat{\mathbb{F}}_n \,\mathrm{d}s = \int_{\partial S_m^c} \mathbb{F}_h^c \cdot \mathbf{n}_{mp} \,\mathrm{d}s - \int_{\partial \omega_c} \left(\mathbb{F}_h^c \cdot \mathbf{n}_{\partial \omega_c} - \mathbb{F}^{*,\mathrm{DG}}_{\partial \omega_c} \right) \psi_m^c \,\mathrm{d}s, \tag{32}$$

we directly get

$$\int_{\partial S_m^c \setminus \partial \omega_c} \widehat{\mathbb{F}}_n \,\mathrm{d}s = \int_{\partial S_m^c \setminus \partial \omega_c} \mathbb{F}_h^c \cdot \mathbf{n}_{mp} \,\mathrm{d}s - \int_{\partial \omega_c} \left(\mathbb{F}_h^c \cdot \mathbf{n}_{\partial \omega_c} - \mathbb{F}^{*,\mathrm{DG}}_{\partial \omega_c} \right) \widehat{\psi}_m^c \,\mathrm{d}s, \tag{33}$$

where $\widehat{\psi}_m^c$ is defined above. We now use a face integrated value of the high-order DG reconstructed flux. Indeed, for a face Γ_{mp}^c, let $\widehat{\mathbb{F}}_{mp}$ be defined as:

$$\int_{\Gamma_{mp}^c} \widehat{\mathbb{F}}_n \,\mathrm{d}s = \varepsilon_{mp}^c \widehat{\mathbb{F}}_{mp},$$

and, similarly, let $\mathbb{F}_{mp}$ be the face integrated value of the polynomial interior flux

$$\int_{\Gamma_{mp}^c} \mathbb{F}_h^c \cdot \mathbf{n}_{mp} \,\mathrm{d}s = \varepsilon_{mp}^c \mathbb{F}_{mp}.$$

Now, considering the vectors $\mathbb{F}_c \in \mathbb{R}^{n_f^c}$ and $\widehat{\mathbb{F}}_c \in \mathbb{R}^{n_f^c}$ defined earlier gets us to the following:

$$\mathbb{A}_c \widehat{\mathbb{F}}_c = \mathbb{A}_c \mathbb{F}_c - \partial \mathbb{F}_c.$$

Remarking that $\mathbb{A}_c$ is not necessarily a square matrix and $\ker \mathbb{A}_c \neq \mathbf{0}$, we make use of the graph Laplacian technique employed in [76], allowing us to solve such system and express explicitly the reconstructed flux $\widehat{\mathbb{F}}_c$ through the interior flux and a boundary correction term. We get the following inverse of $\mathbb{L}_c$ on the orthogonal of its kernel:

$$\mathscr{L}_c^{-1} = (\mathbb{L}_c + \lambda \Pi)^{-1} - \frac{1}{\lambda} \Pi,$$

for any $\lambda \neq 0$, with $\Pi = \frac{1}{N_s}(1 \otimes 1) \in \mathscr{M}_{N_k}(\mathbb{R})$. The reconstructed flux then writes as:

$$\widehat{\mathbb{F}}_c = \mathbb{F}_c - \mathbb{A}_c^\top \mathscr{L}_c^{-1} \partial \mathbb{F}_c.$$

□

References

[1] R. Abgrall. Some remarks about conservation for residual distribution schemes. *Computational Methods in Applied Mathematics*, 18(3):327–351, 2018.

[2] F. Alcrudo and P. Garcia-Navarro. A high-resolution godunov-type scheme in finite volumes for the 2d shallow-water equations. *Internat. J. Numer. Methods Fluids*, 1993.

[3] K. Anastasiou and C. Chan. Solution of the 2d shallow water equations using the finite volume method on unstructured triangular meshes. *Int J Numer Methods Fluids*, 24:1225–1245, 1997.

[4] E. Audusse, F. Bouchut, M.-O. Bristeau, R. Klein, and B. Perthame. A fast and stable well-balanced scheme with hydrostatic reconstruction for shallow water flows. *SIAM J. Sci. Comput.*, 25(6):2050–2065, 2004.

[5] D. Balsara, C. Altmann, C. Munz, and M. Dumbser. A sub-cell based indicator for troubled zones in RKDG schemes and a novel class of hybrid RKDG+HWENO schemes. *J. Comp. Phys.*, 226:586–620, 2007.

[6] S. Barros and J. Cardenas. A nonlinear galerkin method for the shallow-water equations on periodic domains. *J. Comput. Phys.*, 172:592–608, 2001.

[7] A. Bermudez, A. Dervieux, J.-A. Desideri, and M. Vazquez. Upwind schemes for the two-dimensional shallow water equations with variable depth using unstructured meshes. *Comput. Methods Appl. Mech. Engrg.*, 155:49–72, 1998.

[8] C. Berthon and F. Marche. A positive preserving high order VFRoe scheme for shallow water equations: a class of relaxation schemes. *SIAM J. Sci. Comput.*, 30(5):2587–2612, 2008.

[9] C. Berthon, F. Marche, and R. Turpault. An efficient scheme on wet/dry transitions for shallow water equations with friction. *Comput. Fluids*, 48(1):192 – 201, 2011.

[10] R. Biswas, K. D. Devine, and J. E. Flaherty. Parallel, adaptive finite element methods for conservation laws. *Applied Numerical Mathematics*, 14:255 – 283, 1994.

[11] A. Canestrelli, A. Siviglia, M. Dumbser, and E. Toro. Well-balanced high-order centred schemes for non-conservative hyperbolic systems. applications to shallow water equations with fixed and mobile bed. *Advances in Water Resources*, 32(6):634–644, 2009.

[12] S. Cardonna, A. Haidar, F. Marche, and F. Vilar. Local subcell monolithic dg/fv methods for nonlinear shallow-water models with source terms. *Int. J. Numer. Meth. Fluids*, 98(45), 2026.

[13] G. Carrier and H. Greenspan. Water waves of finite amplitude on a sloping beach. *Journal of Fluid Mechanics*, 2:97—109, 1958.

[14] E. Casoni, J. Peraire, and A. Huerta. One-dimensional shock-capturing for high-order discontinuous Galerkin methods. *Int. J. Numer. Meth. Fluids*, 71:737–755, 2013.

[15] M. Castro Diaz, J. Lopez-Garcia, and C. Parès. High order exactly well-balanced numerical methods for shallow water systems. *J. Comput. Phys.*, 246:242–264, 2013.

[16] S. Clain, S. Diot, and R. Loubère. A high-order finite volume method for systems of conservation laws—multi-dimensional optimal order detection (mood). *J. Comput. Phys.*, 230:4028–4050, 2011.

[17] B. Cockburn, S. Hou, and C.-W. Shu. The Runge-Kutta Discontinuous Galerkin Method for Conservation Laws V: Multidimensional Systems. *J. Comp. Phys.*, 141:199–224, 1998.

[18] J. N. de la Rosa and C. D. Munz. Hybrid DG/FV schemes for magnetohydrodynamics and relativistic hydrodynamics. *Comp. Phys. Commun.*, 222:113–135, 2018.

[19] D. A. Di Pietro and A. Ern. *Mathematical Aspects of Discontinuous Galerkin Methods*, volume 69 of *Mathématiques and Applications.* Springer, 2012.

[20] S. Diot, S. Clain, and R. Loubère. Improved detection criteria for the multi-dimensional optimal order detection (MOOD) on unstructured meshes with very high-order polynomials. *Computers and Fluids*, 64:43–63, 2012.

[21] S. Diot, R. Loubère, and S. Clain. The MOOD method in the three-dimensional case: very-high-order finite volume method for hyperbolic systems. *Int. J. Numer. Meth. Fluids*, 73:362–392, 2013.

[22] D.Kuzmin. Slope limiting for discontinuous galerkin approximations with a possibly non-orthogonal taylor basis. *Int J Numer Methods Fluids*, 71(9):1178–1190, 2013.

[23] M. Dumbser and R. Loubère. A simple robust and accurate a posteriorisub-cell finite volume limiter for the discontinuousGalerkin method on unstructured meshes. *J. Comp. Phys.*, 319:163–199, 2016.

[24] A. Duran and F. Marche. Recent advances on the discontinuous Galerkin method for shallow water equations with topography source terms. *Comput. Fluids*, 101:88–104, 2014.

[25] A. Duran, F. Marche, C. Berthon, and R. Turpault. Numerical discretizations for shallow water equations with source terms on unstructured meshes. In A. S. on Applied Mathematics, editor, *Proceedings of the Fourtheenth International Conference on Hyperbolic Problems: Theory Numerics and Applications - HYP 2012, Padova*, volume 8, pages 541–549, 2014.

[26] A. Duran, F. Marche, C. Berthon, and R. Turpault. Asymptotic preserving scheme for the shallow water equations with source terms on unstructured meshes. *J. Comput. Phys.*, 287(184–206), 2015.

[27] K. Erduran, V. Kutija, and C. Hewett. Performance of finite volume solutions to the shallow water equations with shock-capturing schemes. *Int J Numer Methods Fluids*, 40:1237–1273, 2002.

[28] A. Filippini, L. Arpia, V. Perrier, R. Pedreros, P. Bonneton, D. Lannes, F. Marche, S. de Brye, S. Delmas, F. Boulahya, and M. Ricchiuto. An operational discontinuous Galerkin shallow water model for coastal flood assessment. *Ocean Modelling*, 192:102447, 2024.

[29] L. Fraccarollo and E. Toro. Experimental and numerical assessment of the shallow water model for two-dimensional dam-break type problems. *J. Hydraulic Res.*, 33(6):843–863, 1995.

[30] E. Gaburro, W. Boscheri, S. Chiocchetti, and M. Ricchiuto. Discontinuous galerkin schemes for hyperbolic systems in non-conservative variables: Quasi-conservative formulation with subcell finite volume corrections. *Computer Methods in Applied Mechanics and Engineering*, 431:117311, 2024.

[31] J. Gallardo, C. Parés, and M. Castro. On a well-balanced high-order finite volume scheme for shallow water equations with topography and dry areas. *J. Comput. Phys.*, 227(1):574–601, 2007.

[32] S. Gottlieb, C.-W. Shu, and T. E. Strong stability preserving high order time discretization methods. *SIAM Review*, 43:89–112, 2001.

[33] S. Gottlieb, C.-W. Shu, and E. Tadmor. Strong stability-preserving high-order time discretization methods. *SIAM Review*, 43(1):89–112, 2001.

[34] J.-L. Guermond, R. Pasquetti, and B. Popov. Entropy viscosity method for nonlinear conservation laws. *J. Comput. Phys.*, 230:4248–4267, 2011.

[35] J.-L. Guermond, B. Popov, E. Tovar, and C. Kees. Robust explicit relaxation technique for solving the Green-Naghdi equations. *J. Comput. Phys.*, 2019.

[36] M. Guerra, R. Cienfuegos, C. Escauriaza, F. Marche, and J. Galaz. Modeling rapid flood propagation over natural terrains using a well-balanced scheme. *J. Hydraulic Res.*, 140(7), 2014.

[37] A. Haidar, F. Marche, and F. Vilar. A posteriori finite-volume local subcell correction of high-order discontinuous Galerkin schemes for the nonlinear shallow-water equations. *J. Comput. Phys.*, 452:110902, 2022.

[38] A. Haidar, F. Marche, and F. Vilar. Free-boundary problems for wave-structure interactions in shallow-water: Dg-ale description and local subcell correction. *J. Sci. Comput.*, 98(45), 2024.

[39] M. Ioriatti and M. Dumbser. A posteriori sub-cell finite volume limiting of staggered semi-implicit discontinuous Galerkin schemes for the shallow water equations. *Applied Numerical Mathematics*, 135:443–480, 2019.

[40] M. Iskandarani, D. B. Haidvogel, and J. P. Boyd. A staggered spectral element model with application to the oceanic shallow water equations. *Int J Numer Methods Fluids*, 20(5):393–414, 1995.

[41] G. Kesserwani and Q. Liang. Well-balanced RKDG2 solutions to the shallow water equations over irregular domains with wetting and drying. *Comput. Fluids*, 39(10):2040–2050, 2010.

[42] R. Kirby and S. Sherwin. Stabilisation of spectral / hp element methods through spectral vanishing viscosity: Application to fluid mechanics. *Comput. Methods Appl. Mech. Engrg.*, 195:3128–3144, 2006.

[43] L. Krivodonova. Limiters for high-order discontinuous Galerkin methods. *J. Comp. Phys.*, 226:879–896, 2007.

[44] A. Kurganov and G. Petrova. A second-order well-balanced positivity preserving central-upwind scheme for the saint-venant system. *Commun. Math. Sci.*, 5(1):133–160, 2007.

[45] D. Kuzmin. A vertex-based hierarchical slope limiter for p-adaptive discontinuous galerkin methods. *J. Comput. Applied. Math.*, 233(12), 2010.

[46] D. Kuzmin and M. de Luna. Subcell flux limiting for high-order bernstein finite element discretizations of scalar hyperbolic conservation laws. *J. Comp. Phys.*, 411:109411, 2020.

[47] S. Le Roy, R. Pedreros, C. André, F. Paris, S. Lecacheux, F. Marche, and C. Vinchon. Coastal flooding of urban areas by overtopping: dynamic modelling application to the Johanna storm (2008) in Gavres (France). *Nat. Hazards Earth Syst. Sci.*, 15:2497–2510, 2014.

[48] P. Lesaint and P.-A. Raviart. On a finite element method to solve the neutron transport equation. In C. de Boor, editor, *Partial Differential Equations.* Academic Press, New York, 1974.

[49] H. Li and R.-X. Liu. The discontinuous Galerkin finite element method for the 2d shallow water equations. *Mathematics and Computers in Simulation*, 56:223–233, 2001.

[50] L. Li and Q. Zhang. A new vertex-based imiting approach for nodal discontinuous galerkin methods on arbitrary unstructured meshes. *Comput. Fluids*, 159:316–326, 2017.

[51] Q. Liang and F. Marche. Numerical resolution of well-balanced shallow water equations with complex source terms. *Advances in Water Resources*, 32(6):873 – 884, 2009.

[52] Y. Lin and J. Chan. High order entropy stable discontinuous galerkin spectral element methods through subcell limiting. *J. Comp. Phys.*, 498:112677, 2024.

[53] H. Ma. A spectral element basin model for the shallow water equations. *J. Comput. Phys.*, 109(1):133 – 149, 1993.

[54] A. Meister and S. Ortleb. A positivity preserving and well-balanced DG scheme using finite volume subcells in almost dry regions. *Appl. Math. Comp.*, 272:259–273, 2016.

[55] V. Michel-Dansac. A well-balanced scheme for the shallow-water equations with topography. *Computers and Mathematics with Applications*, 72(3):568–593, 2016.

[56] V. Michel-Dansac, C. Berthon, S. Clain, and F. Foucher. A two-dimensional high-order well-balanced scheme for the shallow-water equations with topography and Manning friction. *Computers & Fluids*, 230:105–152, 2021.

[57] V. Michel-Dansac, C. Berthon, S. Clain, and F. Foucher. A two-dimensional high-order well-balanced scheme for the shallow water equations with topography and manning friction. *Computers and Fluids*, 230:105152, 2021. hal-02536791v2.

[58] P. Moujaes and D. Kuzmin. Monolithic convex limiting and implicit pseudo-time stepping for calculating steady-state solutions of the euler equations. *Journal of Computational Physics*, 523:113687, 2025.

[59] I. Navon. Finite-element simulation of the shallow-water equations model on a limited-area domain. *Appl. Math. Modelling*, 3, 1979.

[60] S. Noelle, Y. Xing, and C.-W. Shu. High-order well-balanced finite volume weno schemes for shallow water equation with moving water. *J. Comput. Phys.*, 226(1):29–58, 2007.

[61] H. T. Ozkan-Haller and J.T.Kirby. A fourier-chebyshev collocation method for the shallow water equations including shoreline. *Applied Ocean Research*, 19:21–34, 1997.

[62] P.-O.Persson and J.Peraire. Sub-cell shock capturing for discontinuous galerkin methods. *AIAA Aerospace Sciences Meeting and Exhibit*, 112, 2006.

[63] J. Patera and V. Nassehi. A new two-dimensional finite element model for the shallow water equations using a lagrangian framework constructed along fluid particle trajectories. *Int. J. Numer. Meth. Fluids*, 39:4159–4182, 1996.

[64] J. Qiu and C.-W. Shu. A comparison of troubled-cell indicators for Runge-Kutta discontinuous Galerkin methods using weighted essentially nonoscillatory limiters. *SIAM J. Sci. Comput.*, 27:995–1013, 2005.

[65] J. Qiu and C.-W. Shu. Runge Kutta discontinuous Galerkin method using WENO limiters. *SIAM J. Sci. Comput.*, 26:907–929, 2005.

[66] W. Reed and T. Hill. Triangular mesh methods for the neutron transport equation. *Los Alamos Scientific Laboratory Report*, LA-UR-73-479, 1973.

[67] B. Rogers, A. Borthwick, and P. Taylor. Mathematical balancing of flux gradient and source terms prior to using Roe's approximate riemann solver. *J. Comput. Phys.*, 192:422–451, 2003.

[68] A. Rueda-Ramirez, B. Bolm, D. Kuzmin, and G. Gassner. Monolithic convex limiting for legendre-gauss-lobatto discontinuous galerkin spectral-element methods. *Commun. Appl. Math. Comput.*, 2024.

[69] A. M. Rueda-Ramirez, W. Pazner, and G. J. Gassner. Subcell limiting strategies for discontinuous galerkin spectral element methods. *Computers and Fluids*, 247:105627, 2022.

[70] M. Sonntag and C. Munz. Shock capturing for discontinuous Galerkin methods using finite volume subcells. In *Finite Volumes for Complex Applications VII-Elliptic, Parabolic and Hyperbolic Problems*, pages 945–953, 2014.

[71] E. Toro. *Shock-capturing methods for free-surface shallow flows.* Chichester: John Wiley and Sons, 2001.

[72] T. Utnes. A finite element solution of the shallow-water wave equations. *Appl. Math. Modelling*, 14:20–29, 1990.

[73] J. Van der Vegt and H. Van der Ven. Space-time discontinuous Galerkin finite element method with dynamic grid motion for inviscid compressible flows. *J. Comput. Phys.*, 182:546–585, 2002.

[74] F. Vilar. A posteriori correction of high-order discontinuous galerkin scheme through subcell finite volume formulation and flux reconstruction. *J. Comput. Phys.*, 387:245–279, 2019.

[75] F. Vilar. Local subcell monolithic DG/FV convex property preserving scheme on unstructured grids and entropy consideration. *J. Comput. Phys.*, 521(1), 2025.

[76] F. Vilar and R. Abgrall. A posteriori local subcell correction of high-order discontinuous galerkin scheme for conservation laws on two-dimensional unstructured grids. *SIAM Journal on Scientific Computing*, 46(2):A851–A883, 2024.

[77] S. Vukovic. Eno and weno schemes with the exact conservation property for one-dimensional shallow water equations. *J. Comput. Phys.*, 179(2):593–621, 2002.

[78] X. Wu, N. Trask, and J. Chan. Entropy stable discontinuous galerkin methods for the shallow water equations with subcell positivity preservation. *Numerical Methods for Partial Differential Equations*, 40(6):e23129, 2024.

[79] Y. Xing and X. Zhang. Positivity-preserving well-balanced discontinuous Galerkin methods for the shallow water equations on unstructured triangular meshes. *J. Sci. Comput.*, 57:19–41, 2013.

[80] Y. Xing, X. Zhang, and C.-W. Shu. Positivity-preserving high order well-balanced discontinuous galerkin methods for the shallow water equations. *Advances in Water Resources*, 33(12):1476 – 1493, 2010.

[81] J. Zhu, J. Qiu, C.-W. Shu, and M. Dumbser. Runge–Kutta discontinuous Galerkin method using WENO limiters II: Unstructured meshes. *J. Comput. Phys.*, 227:4330–4353, 2008.

[82] J. Zhu, X. Zhong, C.-W. Shu, and J. Qiu. Runge Kutta discontinuous Galerkin method using a new type of WENO type limiters on unstructured meshes. *J. Comp. Phys.*, 248:200–220, 2013.